

Masterarbeit

zur Erlangung des Hochschulgrades
Master of Science
im Master-Studiengang Physik

Studies of a Proton Bunch Monitor for Range Verification in Proton Therapy

Theresa Werner

geboren am 29.08.1989 in Lauchhammer

TECHNISCHE UNIVERSITÄT DRESDEN
INSTITUT FÜR KERN- UND TEILCHENPHYSIK
FACHRICHTUNG PHYSIK
FAKULTÄT MATHEMATIK UND NATURWISSENSCHAFTEN

31.07.2015

Eingereicht am 31. Juli 2015

1. Gutachter: Prof. Dr. A. Straessner
2. Gutachter: Prof. Dr. W. Enhardt

Zusammenfassung

Eine derzeitige Hauptaufgabe im Forschungsbereich der Partikeltherapie ist die Kontrolle sowie die Sicherung einer präzisen Bestrahlung des Zielvolumens. Die Prompt Gamma Timing (PGT) Methode bietet unter anderem die Möglichkeit einer in vivo Reichweitenverifikation während der Bestrahlung des Patienten. Dabei wird die Emissionsverteilung von hochenergetischen Photonen genutzt um die Eindringtiefe der primären Protonen zu bestimmen. Durch Kernwechselwirkungen des Projektils mit Materie werden Photonen erzeugt und prompt emittiert, welches zusätzlich die Möglichkeit bietet eine Echtzeitinformation der Reichweite zu generieren.

Die Ankunftszeit der Photonen in einem Detektor spiegelt den Abbremsvorgang der primären Protonen im Gewebe wider und ist mit ihrer Eindringtiefe korreliert. Die Zeitauflösung des Detektors und des Protonen Bunches sowie das Driften des Bunches im Bezug auf die Beschleuniger Frequenz führen jedoch zu einer Verschmierung der Zeitspektren und verringern die gewünschte Präzision der Reichweitenbestimmung im Hinblick auf zukünftige klinische Anwendungen.

Um diese Limitierung zu vermeiden und eine robuste Reichweiteninformation aus den PGT Spektren zu regenerieren, kann ein Bunch Monitor eingesetzt werden. Ein erster Prototyp wurde unter anderen an der GSI Darmstadt bei Messungen des Energieprofils von gestreuten Ionen getestet. Am ELBE Beschleuniger, welcher Bremsstrahlungsphotonen in sehr kurzen Pulsen generiert, wurde zur Optimierung der Zeitauflösung ein Constant Fraction Algorithmus für die digital gemessenen Signale evaluiert. Streuexperimente mit verschiedenen Targets und Detektorpositionen an einem klinischen Protonen Strahl (OnocRay, Dresden) erlauben eine grundlegende Charakterisierung der Protonen Bunch Struktur und der Ausbeute an gestreuten Protonen.

Abstract

A focus in current research in particle therapy is the assurance of the precise irradiation of the target volume. The Prompt Gamma Timing (PGT) method provides one possibility for in vivo range verification during patient treatment. This approach exploits the emission distribution of gamma rays with high energies to determine the penetration depth of the primary protons. The photons are emitted promptly due to nuclear reactions of the projectile with tissue.

Their arrival time on a detector reflects the stopping process of the primary protons in tissue and is directly correlated to the range. Due to the timing resolution of the detector and the proton bunch time spread, as well as drifts of the bunch phase with respect to the accelerator radio frequency, timing spectra are smeared out and compromise the accuracy of range information intended for future clinical applications. Nevertheless, counteracting this limitation and recovering range information from the PGT measured spectra, corrections using a phase bunch monitor can be performed. A first prototype of a bunch monitor was tested at GSI Darmstadt, where measurements of the energy profile of the ion bunches were performed. At the ELBE accelerator at Helmholtz-Zentrum Dresden-Rossendorf (HZDR), set up to provide bremsstrahlung photons in very short pulses, a constant fraction algorithm for the sampled digital signals was evaluated, which is used for optimizing the timing resolution. Scattering experiment studies with different thin targets and detector positions are accomplished at OncoRay Dresden, where a clinical proton beam is available. These experiments allow a basic characterization of the proton bunch structure and the detection yield.

Contents

List Of Abbreviations	ix
List Of Figures	xii
List Of Tables	xiii
1 Introduction	1
1.0.1 Motivation of the Thesis	2
1.0.2 Aim	4
2 Physical Background	5
2.1 Kinematics	6
2.2 Interaction of Protons with Matter	7
2.2.1 Interaction with the Atomic Shell	7
2.2.2 Interaction with the Atomic Nuclei	8
2.3 Principle of Prompt Gamma Timing	11
2.4 Proton Accelerators	12
2.5 Scintillation Detector Principles	15
2.5.1 Organic Scintillators	15
2.5.2 Inorganic Scintillators	17
2.6 Phoswich Detector	19
2.6.1 Pulse Timing Methods	20
2.6.2 Pulse Shape Discrimination	21
3 Concept	23
3.1 Digital Pulse Processing	23
3.2 Materials and Methods	25
3.3 Bunch Monitoring	29
4 Experiments and Results	33
4.1 Preparatory Experiments	34
4.1.1 SIS18 Synchrotron at GSI Darmstadt	34
4.1.2 ELBE Linear Accelerator at HZDR	36
4.2 C230 Cyclotron at OncoRay Dresden	39
4.2.1 Energy Calibration and Particle Identification	39
4.2.2 Time Width and Yield Measurements	45
4.2.3 Energy Straggling and Detector Timing Resolution	48
5 Conclusion and Outlook	53

List of Abbreviations

ADC	analog-to-digital converter
BGO	bismuth germanium oxide
CFD	constant fraction discriminator
DNA	deoxyribonucleic acid
DPP	digital pulse processing
DPP-PSD	digital pulse processing - pulse shape discrimination
FWHM	full width at half maximum
MCS	multiple coulomb scattering
PET	positron emission tomography
PGI	Prompt Gamma Imaging
PGT	Prompt Gamma Timing
PMT	photomultiplier tube
PMMA	polymethyl methacrylate
PSD	pulse shape discrimination
RF	radio frequency

List of Figures

1.1	Illustration of a critical dose deposition.	1
1.2	Illustration of signatures used for range verification.	2
1.3	Slit camera setup with simulated particle tracks.	3
1.4	Scheme of the operating principle of the Compton camera.	4
2.1	Dose distribution of 140 MeV protons in water.	5
2.2	Range of protons in different materials.	6
2.3	Correlation between kinetic energy and reduced wavelength for different particles.	7
2.4	Specific energy loss of protons in polymethyl methacrylate.	8
2.5	Angular dependence of the Rutherford cross section.	9
2.6	Schematic illustration of various nuclear reactions.	10
2.7	Scheme of the Prompt Gamma Timing method.	11
2.8	Operation of a cyclotron.	13
2.9	The C230 Cyclotron of the company IBA.	14
2.10	Energy levels of an organic molecule.	16
2.11	Scintillation light yield of a plastic scintillator.	17
2.12	Mechanism of an inorganic scintillator.	18
2.13	Measurements of the light pulse shapes from BGO.	18
2.14	Emission spectra of inorganic scintillators.	19
2.15	Scheme of an expected energy correlation spectrum of a phoswich detector.	20
2.16	Illustration of constant fraction timing and leading edge trig- gering.	20
2.17	Illustration of pulse shape discrimination.	21
3.1	Illustration of a sampled waveform with the most important software parameters.	24
3.2	Experimental setup of a bunch phase monitor system.	25
3.3	Scheme of a phoswich detector for charged particle identification.	25
3.4	Superposition of recorded waveforms with a phoswich detector.	27
3.5	Scheme of the operating principle of the online CFD.	27
3.6	Energy correlation spectra with an online energy cut.	28
3.7	Energy correlation spectra with an online energy cut.	28
3.8	Typical energy correlation spectra of a scattering experiment with protons recorded with a phoswich detector.	29
3.9	Extraction of the primary proton bunch structure parameters.	30
3.10	Prompt Gamma Timing with a bunch monitor.	31
4.1	Picture of the experimental setup at GSI.	34
4.2	Correlation of energy loss and residual energy measured at GSI.	35
4.3	Experimental setup at the ELBE accelerator.	36
4.4	Spectra of bremsstrahlung photons measured at ELBE (HZDR).	36
4.5	Time walk correction of a recorded photon spectrum.	37

4.6	Mean peak position of the measured photon arrival time. . . .	38
4.7	Time width of bremsstrahlung photons measured at ELBE. . .	38
4.8	Scheme of the experimental setup for first scattering experiments.	39
4.9	Recorded energy correlation spectra of scattered protons on polyethylene.	40
4.10	Energy calibration based on elastic scattering processes of different incident energies.	41
4.11	Measured specific energy loss as a function of different incident energies compared to the theoretical values from NIST reference database.	42
4.12	Energy bunch width of scattered protons as a function of their kinetic energy.	42
4.13	Scheme of the experimental setup for time of flight measurements.	43
4.14	Different energy and time spectra of scattered protons/deuteron.	44
4.15	Setup of the scattering experiment for investigation of the detection yield.	45
4.16	Energy correlation and coincidence time spectra of a clinical proton beam.	46
4.17	The mean <i>FWHM</i> of the timing signal of scattered protons with different incoming energies.	46
4.18	Total counts of elastically scattered protons on different targets.	47
4.19	Scheme of the experimental setup.	48
4.20	A recorded energy over time correlation spectra.	48
4.21	Linear energy calibration.	49
4.22	Illustration of the effect of the respective bunch structure parameters on the spectra.	49
4.23	Mean <i>FWHM</i> of the timing signal of protons with different initial kinetic energies E_{kin}	50
5.1	Measured slopes of the different energy peaks.	54
5.2	Experimental setup in the treatment room.	56
5.3	Proton energy spectra measured in the treatment room.	57
5.4	Count rate of protons measured in the treatment room.	57
5.5	Various spectra measured with the digital data acquisition system.	58

List of Tables

2.1	Timing properties of fast plastic scintillators	16
2.2	Decay times of some scintillator materials	19
4.1	Transit time values for protons and secondary particles.	43
4.2	Theoretical and experimental values of the peak slope.	51

Chapter 1

Introduction

The combination of modern medicine with the considerable technical progress in accelerator technology, as well as the interdisciplinary collaboration of scientists around the world, open the possibility to cure serious diseases such as cancer. This trend, for instance, is reflected in the advances in radiation therapy using the special properties of charged particles. Compared to conventional cancer therapy, such as the treatment of tumors using photons, particle therapy with protons or heavy ions offers considerable advantages. In contrast to photons, which are conventionally used in radiation therapy, protons have a distinct range in tissue. The incident particles deposit their energy within the tissue, which leads to a breaking of the deoxyribonucleic acid (DNA) with, at best, a subsequent apoptosis of malignant tumor cells. Because of the self repairing mechanism of the cells to a certain extent, it must be ensured that enough dose is delivered in the target volume. Therefore, the resulting main challenge in tumor therapy is to destroy the tumor cells, while sparing the surrounding healthy tissue [1].

For this, the dose deposition profile of protons and heavy ions can be exploited. This distribution is characterized by a distinct maximum (Bragg Peak) near the end of the particle range and a subsequent sharp fall-off of the dose deposition. These properties allow to treat tumors near sensitive healthy organs. A main subject of current medical research in this promising form of therapy is to ensure the precise irradiation of the target volume. It is important to avoid an accidental overdose in healthy tissue (especially in regions at risk) or a possible underdose in the tumor (figure 1.1).

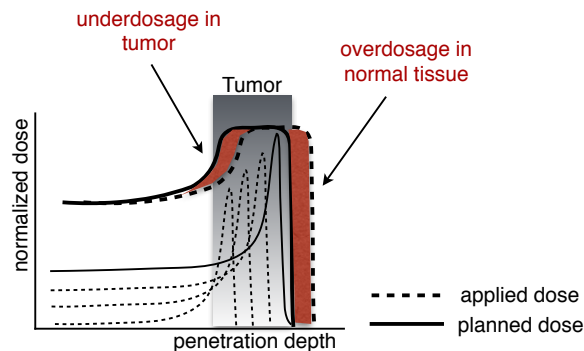


Figure 1.1: Tumor treatment with protons of different penetration depth. The solid line characterizes the planned dose distribution while the dashed line shows the indeed applied dose. The red areas indicate a critical underdose in the tumor or rather an overdose outside the tumor region.

Besides the incident energy, the penetration depth depends on the density and the composition of the tissue along the particle track. Uncertainties are caused by patient positioning, anatomical and physiological changes, organ motion and implants as well as the lateral scattering process in a complex anatomy. Furthermore, an independent control system for important beam parameters could detect an inadequate modeling of the beam profile in clinical applications. Consequently, it is of high interest to verify the range during the treatment and to examine special beam parameters [2].

1.0.1 Motivation of the Thesis

In order to increase the quality of particle therapy, there are several strategies to determine the particle range in tissue during the treatment of patients, which counteracts these accidental dose depositions as mentioned above. A direct measurement by detecting the particles is not possible as they do not leave the patient. Therefore, signatures from nuclear interaction processes of the projectile with the target can be exploited (figure 1.2).

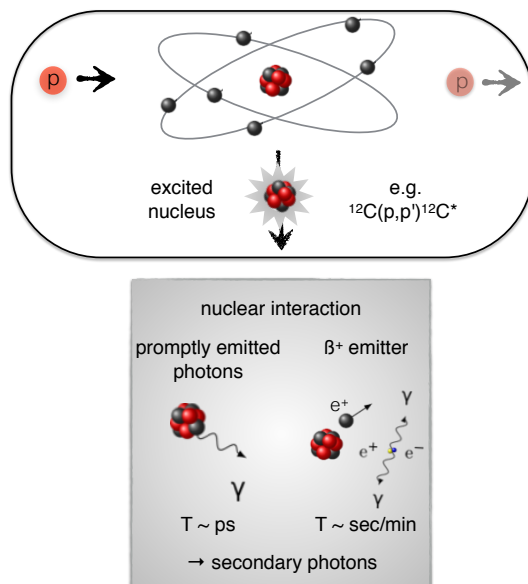


Figure 1.2: Illustration of signatures from nuclear interaction used for range verification.

A currently clinically established method, the positron emission tomography (PET), takes profit of the resulting beta plus (β^+) decay from a positron-emitting radionuclide, which is produced in inelastic nuclear reactions. The system detects and localizes the back-to-back annihilation photons to form an image that reflects the actual locations of the radioactive atoms. The simultaneously produced photons have an energy of 511 keV with a respective inverse momentum. Due to the long decay time ($\sim \text{sec/min}$), it is not possible to get a real-time information of the particle range. Additionally, the blood flow leads to washout effects and degrades, combined with the low statistic, the range information. A detailed description of this procedure can be found in [3].

Besides these photons, gamma rays with high energies ($\sim \text{MeV}$) are emitted promptly ($\sim \text{ps}$) due to nuclear reactions between protons and the nuclei in tissue. Systems, which extract the range information by analyzing the spatial distribution of these gammas, are for example the passively collimated slit camera [4] or the actively collimated Compton camera [5].

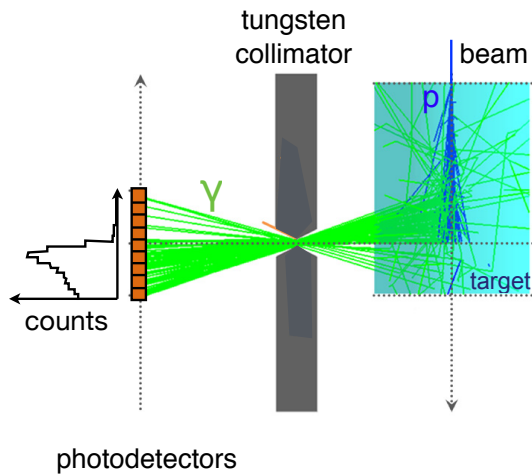


Figure 1.3: A possible slit camera setup with simulated particle tracks. The green lines indicate the produced prompt photons and the blue line belongs to the primary protons. The different count rates in the segmented detector lines (highest count rate closed to the Bragg peak) allows a range assessment in one dimension [4].

The slit camera produces a reverse 1D image of the emission pattern by a knife-edge slit collimator. The segmented detector lines have different count rates (highest count rate closed to the Bragg peak), caused by the spatial emission distribution (figure 1.3). The recorded profile correlates with the penetration depth of the primary protons, but allows only a range assessment in one dimension. Due to the tungsten collimator the experimental setup has a high weight (~ 50 Kg).

The Compton camera system is based on the classical Compton scattering formalism and typically consists of a scattering detector and an absorber detector. The origin of the emitted prompt photons can be reconstructed through a measurement of energy and interaction positions in the respective detector modules. If the interaction position in both detectors and the incident energy of the photon is known, it is possible to reconstruct cones containing their incident trajectories. Thereby, the top of the cone is the interaction point in the scatterer detector, which also determines with the interaction point in the absorber detector, the axis of the cone. Finally, the system produces an image by overlaying different cones, which are determined by each detected single event (figure 1.4).

The efficiency is mainly limited through the coincidence nature of the photons in the two detector stages, because random coincidences caused by the high background counteract the valid events. It is also a complex and expensive system due to highly granular detectors and electronics. Further information of these methods can be found in [4] (slit camera) and in [6] (Compton camera).

Besides these Prompt Gamma Imaging (PGI) systems, the Prompt Gamma Timing (PGT) method provides one possibility for in vivo range verification based on conventional timing spectroscopy. The primary proton bunches pass the beam nozzle, enter the target and prompt photons are emitted along the particle track. The proton transit time through the target volume (body) is of the order of 1 ns. As mentioned above, it is not possible to directly measure the beam position by detecting the protons, but the emitted photons leave the target. The arrival time of the prompt photons at the detector reflects the

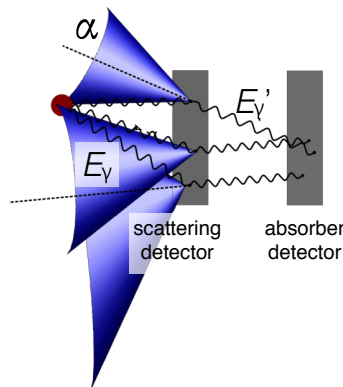


Figure 1.4: The origin of the emitted prompt photons can be reconstructed through a measurement of energy deposition and interaction positions in the respective detector modules. The system produces an image by overlaying different cones, which are determined by each detected single event [6].

stopping process of the primary protons in the tissue and is directly correlated to the range. The longer the proton range, the longer prompt photons are emitted.

Due to the timing resolution of the detector and the proton bunch time spread, as well as drifts of the bunch phase with respect to the accelerator frequency, timing spectra are smeared out and compromise the accuracy of range information intended for future clinical applications. Therefore, in contrast to the constant detector timing resolution, it must be monitored on-line. Furthermore, an unstable bunch phase with respect to the accelerator may additionally shift and smear the profile and compromise the accuracy and robustness of PGT. In order to counteract this limitation a phase bunch monitor can be used and range information from the corrected PGT spectra can be recovered [7], [8].

1.0.2 Aim

This thesis presents the first studies of a bunch monitor prototype for increasing the robustness of the PGT method, under consideration of the requirements in future medical applications. For first investigations a detector, which operates according to the phoswich principle, combined with a digital data acquisition, to minimize the technical equipment, is used. The following specific task were examined:

- (a) The selection and preparation of a detector which has a suitable size for clinical application and, at the same time, is still able to measure high energetic charged particles. Moreover, it needs a reasonable time resolution referred to previous published measurements in the range of ~ 400 ps.
- (b) The configuration of the digital data acquisition software, which includes the exploration of different pulse shape discrimination parameters, as well as an algorithm for analyzing the time structure of the waveform.
- (c) Various scattering experiments with the assembled experimental setup in order to verify, whether it is possible to use it as a bunch monitor.

Chapter 2

Physical Background

When a proton or heavy ion travels through material, it will have a certain probability of interacting with the orbital electrons or the nuclei by electromagnetic or nuclear forces, respectively. During this process, it will transfer some of its energy to the participating particle. The total energy deposited in a mass element, which is mainly dominated by the specific energy loss of the proton in matter, is given by the absorbed dose (equation 2.1) where the SI unit is Gray [$1 \text{ Gy} = 1 \text{ J/kg}$].

$$D = \frac{d\epsilon}{dm} \quad [1 \text{ Gy} = 1 \text{ J/kg}] \quad (2.1)$$

The characteristic dose distribution of protons in matter (figure 2.1), leads to a well-defined proton range in tissue and offers the possibility for treating deep seated tumors surrounded by organs at risk. Additionally, the ongoing development of powerful and compact particle accelerators guarantees the opportunity to use this special, physical behavior in cancer treatment. In order to fulfill medical requirements and to develop methods which ensure the quality of particle therapy, it is important to understand the fundamental particle interaction processes as well as the accelerator behavior.

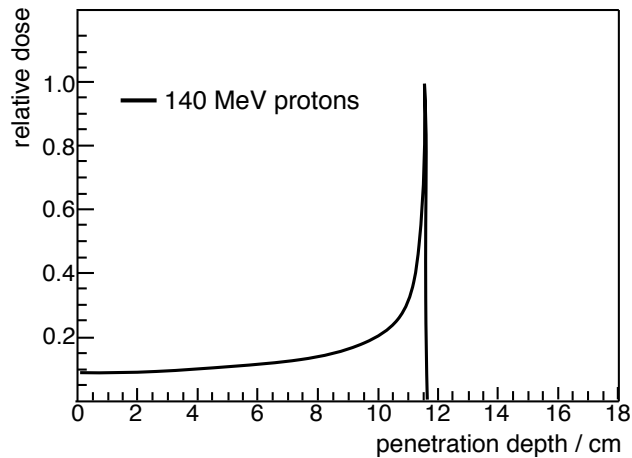


Figure 2.1: The dose distribution of 140 MeV protons in water [9]. Protons traveling through matter have a well-defined range.

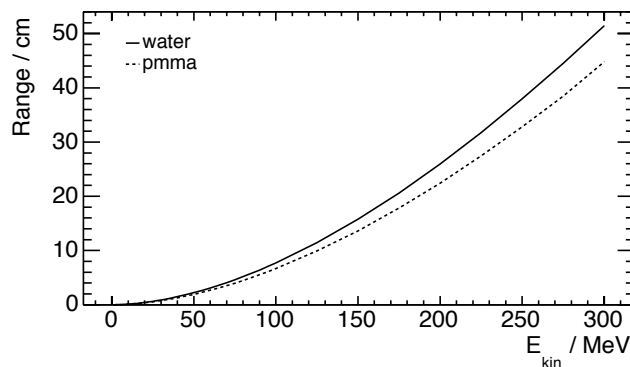


Figure 2.2: Range of protons in water and PMMA [10]. In radiation therapy penetration depths of up to 30 cm are required. Consequently, the kinetic energy of protons used for treatment is in the range of 3-300 MeV.

2.1 Kinematics

Figure 2.2 shows the penetration depth of protons in acrylic glass (polymethyl methacrylate (PMMA)) ($C_5O_2H_8$) and water depending on their kinetic energy E_{kin} [10]. In radiotherapy, penetration depths of up to 30 cm are required to treat deep-seated tumors in the body. This depth, assuming water equivalent tissue, can be achieved with an incoming proton energy of $E_{\text{kin}} = 217.5$ MeV. Consequently, the typical energy spectra of protons in radiotherapy ranges from 3 MeV - 300 MeV [1].

Protons are not elementary particles and have a substructure consisting of quarks and gluons. In quantum mechanics, every particle is associated with a De-Broglie wavelength $\lambda = \frac{h}{p}$. To resolve structures with a linear extension Δx , the reduced wavelength has to be in the same order of magnitude: $\Delta x \approx \lambda$. Figure 2.3 shows the correlation between the kinetic energy and the reduced wavelength for different particles. At high momenta (\sim several GeV/c), the wavelength of the projectile is less than fm and it is possible to decompose the constituents of the nuclei [11].

According to equation 2.2, medical protons have a De-Broglie wavelength between $0.25 \text{ fm} \lesssim \lambda \lesssim 2.66 \text{ fm}$. These protons can resolve the nucleus (diameter $\sim 10^{-15} \text{ m} = 1 \text{ fm}$).

$$\lambda = \frac{h}{p} = \frac{hc}{\sqrt{2mc^2 E_{\text{kin}} + E_{\text{kin}}^2}} \approx \begin{cases} \hbar/\sqrt{2mE_{\text{kin}}}, & \text{if } E_{\text{kin}} \ll mc^2 \\ \hbar c/E_{\text{kin}} \approx \hbar c/E & \text{if } E_{\text{kin}} \gg mc^2 \end{cases} \quad (2.2)$$

The energy E of the protons follows the relativistic energy-momentum relation:

$$E^2 = (pc)^2 + (m_0 c^2)^2 \quad (2.3)$$

with the relativistic momentum p :

$$p = \gamma m v \quad \gamma = \frac{1}{\sqrt{1 - (\frac{v}{c})^2}} \quad (2.4)$$

The resulting energy-dependent velocity is given by

$$v(E_{\text{kin}}) = \frac{dx}{dt} = c \sqrt{1 - \left(\frac{m_0 c^2}{E_{\text{kin}} + m_0 c^2} \right)^2} \quad (2.5)$$

and the transit time t to pass a distance $\Delta x = x - x_0$ by

$$t(x) = \int_{x_0}^x \frac{1}{v(E_{\text{kin}}(x))} dx \quad (2.6)$$

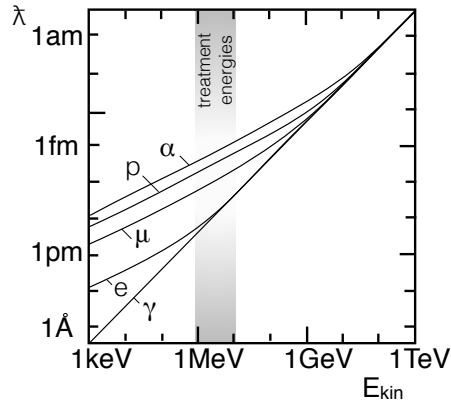


Figure 2.3: Correlation between kinetic energy E_{kin} and reduced wavelength λ for photons (γ), electrons (e), muons (μ), protons (p) and He-cores (α). The diameter of an atom is typically in the range of angstrom \AA (10^{-10} m), and the nuclei of fm (10^{-15} m) [11].

For example, a proton with a kinetic energy $E_{\text{kin}} = 160$ MeV has a velocity of $v \approx 0.27c$.

According to equation 2.4, medical protons have a momentum of $p(E_{\text{kin}} = 5 \text{ MeV}) = 97 \text{ MeV}/c$ up to $p(E_{\text{kin}} = 230 \text{ MeV}) = 696 \text{ MeV}/c$. In this low energy range, the proton behaves like an elementary particle with no substructure [1].

2.2 Interaction of Protons with Matter

2.2.1 Interaction with the Atomic Shell

Charged particles like electrons, protons or heavier ions are surrounded by their electromagnetic field. The mutual interaction between charged particles occur in single collisions leading to ionization, atomic or collective excitation. In a macroscopic piece of matter, the probability for that is close to 100 %. If only one single process is taken into consideration, then the transferred energy is very low ($\Delta E \approx 100$ eV in 90% of all collisions). Consequently, many interactions are necessary for stopping a projectile in matter [12].

The macroscopic formalism, which consolidates these single scattering events for heavy particles is described by the Bethe Bloch formula (equation 2.7).

$$-\left\langle \frac{dE}{dx} \right\rangle = K \rho z^2 \frac{Z}{A} \frac{1}{\beta^2} \left(\frac{1}{2} \ln \frac{2m_e c^2 \beta^2 \gamma^2 \Delta T_{\text{max}}}{I^2} - \beta^2 - \frac{\delta(\beta\gamma)}{2} - \frac{C}{Z} \right) \quad (2.7)$$

with:

- m_e : electron mass
- K : $\approx 0.31 \text{ MeV g}^{-1} \text{ cm}^2$
- z, β : electric charge and velocity of the incoming particle
- Z, A : charge and mass number
- ρ : density of the material
- I : mean excitation potential
- ΔT_{max} : maximum energy transfer (central scattering)
- $\delta(\beta\gamma)$: density corrections at high energies
- C/Z : shell corrections at low energies

The mean rate of energy loss between heavy charged particles with the orbital electrons of the target atoms increases as the projectile slows down. Accord-

ing to the estimated momentum in section 2.1, the specific energy loss of protons used for radiotherapy is described by the linear portion of the curve (figure 2.4), where relativistic corrections can be neglected. In simple terms, it means that the momentum transferred to the electron is higher the longer the proton perceives the field of the electron. Therefore, the mean projected range $\langle R \rangle$ (proportional to the penetration depth) of the energy loss expectation value $-\langle \frac{dE}{dx} \rangle$ (equation 2.8) is approximately proportional to the kinetic energy squared, where E_0 is the incoming energy.

$$\langle R \rangle = \int_{E_0}^0 \left(\left\langle \frac{dE}{dx} \right\rangle \right)^{-1} dE \sim E_{\text{kin}}^2 \quad (2.8)$$

The resulting range in tissue for clinical applications can thus be varied by kinetic energy changes of the incoming primary protons. The approximative formula 2.7 is valid in the interval of $0.1 \lesssim \beta\gamma \lesssim 1000$ and an intermediate Z of the material. The product of the two quantities $\beta\gamma$ for protons used in radiotherapy ($E_{\text{kin}} = 5 \text{ MeV} - 230 \text{ MeV}$) is $\beta\gamma = 0.1 - 0.48$.

Atoms in an excited state after interaction can return to the ground state by emitting photons in the range of eV - keV, which causes part of the background in measurements.

2.2.2 Interaction with the Atomic Nuclei

Protons and neutrons which make up the nucleus are themselves considered to be made up of quarks. Atomic nuclei interact through attractive nuclear forces (range in the area of femtometer) or repulsive Coulomb forces (infinite range). In most cases, these processes superimpose in the experiment.

Depending on the studied phenomenology in particle therapy, the elastic or inelastic interaction of the target and the projectile play different roles. Important for later studies of the primary proton bunch structure are especially the elastic scattering processes. In contrast to that, inelastic nuclear reactions, which produce prompt photons and secondary particles, are mainly of interest for range verification.

Elastic Nuclear Scattering

The elastic scattering through the electrostatic interaction of charged particles with the atomic nuclei is described by the Rutherford scattering formalism. If a parallel current of protons collide with a thin target, the particles are

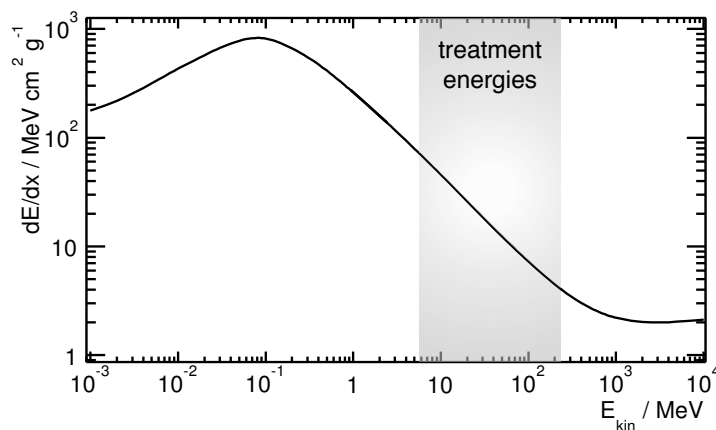


Figure 2.4: The specific energy loss dE/dx of protons in PMMA depending on their kinetic energy E_{kin} [10].

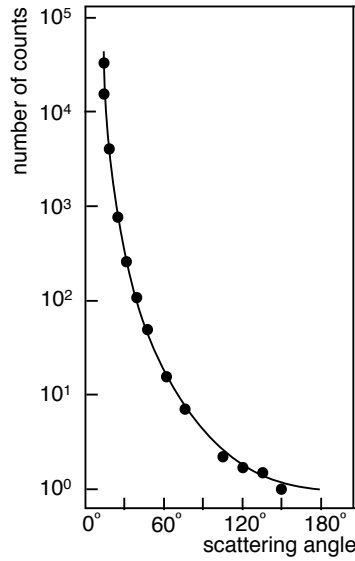


Figure 2.5: Angular dependence of the Rutherford cross section [13].

scattered due to the pure Coulomb potential and will be detected at a defined distance r at an angle Θ . The differential cross section defined as:

$$\frac{d\sigma}{d\Omega} = \frac{\text{number of scattered particles in } d\Omega/s}{\text{current density of the incident particles}} \quad (2.9)$$

determines the number of detected particles with a detector of an area dF in a solid angle element $d\Omega = dF/r^2$ divided by the particle current density. The Rutherford cross section with the Coulomb potential $V(r) = ZZ'e^2/4\pi\epsilon_0 r$, acting simultaneously on two point charges (electrical charge Z, Z'), depends on the energy E of the incoming particle and is given in equation 2.10 [11].

$$\frac{d\sigma}{d\Omega} = \frac{1}{4\pi\epsilon_0} \frac{ZZ'e^2}{4E} \frac{1}{\sin^4(\Theta/2)} \quad (2.10)$$

The cross section, as shown in figure 2.5, increases for a smaller scattering angles over many orders of magnitude.

Depending on the mass of the target nuclei and the impact parameter, the elastic scattering leads to a more or less larger angular deflection. The simplest approach to describe the kinematic of elastically scattered protons in a plane is the classical energy and momentum conservation. The resulting kinetic energy (velocity (v'_1)) of an incoming proton scattered on an atomic nucleus at rest is:

$$\begin{aligned} m_1 = m_2 : & \quad v'_1 = v_1 \cos \Theta'_1 \\ m_1 \neq m_2 : & \quad v_1'^2(m_1 + m_2) \\ & \quad + v_1'(-2m_1 v_1 \cos \Theta_1) = 0 \end{aligned}$$

For example, if a proton collides with a hydrogen nucleus at an angle of 45° , it transfers half of its kinetic energy.

Inelastic Nuclear Reactions

Inelastic nuclear reactions can leave the nucleus as well as the projectile in an excited state, which later decays by photon emission or some other forms of radiation. As mentioned in section 2.1 at energies relevant for particle therapy interactions with the constituents of the nuclei (quarks and gluons) can be neglected. For range verification in particle therapy, especially the excitation of discrete levels with a followed gamma ray emission is of special interest [13]. Elements in tissue are mostly hydrogen, oxygen and carbon with the correlated gamma ray emission energies of 2.2 MeV ($^1\text{H}(n,\gamma)^2\text{H}$), 4.44 MeV (^{16}O and ^{12}C de-excitation) and 6.1 MeV, 6.916 MeV, 7.115 MeV (^{16}O de-excitation) [14]. Another approach in this field (section 1.0.1 (PET)) takes advantage of 511 keV annihilation photons, which originate from the decay of beta plus emitters in inelastic nuclear reactions. A proton inside a radioactive nucleus is converted into a neutron while releasing a positron and an electron neutrino. The positron annihilates in a certain distance with a surrounding electron and produces two photons.

Protons, which enter the nucleus and knock out constituents produce further secondary particles. Figure 2.6 shows some examples of these reactions.

At therapy energies, possible secondary particles are protons, neutrons, γ -rays and recoil residual nuclei. Heavier fragments like alpha particles are quite rare [1]. Because of the low kinetic energies, the secondary particles are scattered with a large angle and should be considered when some scattering or absorber material is in the beam line.

Besides these processes, interactions can also lead to a so called compound nucleus, in which the projectile and the nucleus fuse together and reach a highly excited state. The following de-excitation is achieved by fission, gamma emission or particle fragmentation [13].

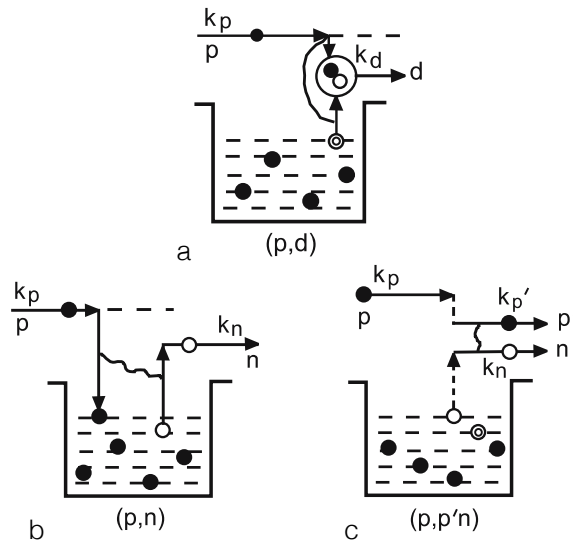


Figure 2.6: Schematic illustration of nuclear proton reactions: (a) pickup reaction, (b) kickoff reaction, (c) knock-on reaction [13].

2.3 Principle of Prompt Gamma Timing

Due to differences in physical interaction processes with matter, proton therapy is much more sensitive to changes in tissue composition compared to conventional photon therapy. The planned dose distribution is mainly defined by the Bragg Peak, and a significant deviation of its position in the target volume could lead to severe side effects. Therefore in clinical practice, it is desirable to control the beam range in vivo during the treatment.

As mentioned in section 1.0.1 PGI takes advantage of the emission nature of the photons and provides a real time information. A special feature of another system called PGT, is the simple experimental setup as well as it dispenses with passive or active collimation elements. The PGT method is based on conventional timing spectroscopy of differences between the time when the particle bunch passes a reference plane (e.g. entrance in the target) and the arrival of the correlated prompt gamma rays to the detector.

The particles in tissue need a finite time (~ 1 ns) to pass the target volume, wherein they produce photons along their track. Obviously, the length of this time is directly correlated with the range in the target (figure 2.7). The transit time t_{transit} depends on the particle velocity $v(E_{\text{kin}})$, the stopping power of the material $S(E_{\text{kin}})$ and the mass density $\rho(x)$ (equation 2.11). If the kinetic energy E_{kin} of the incoming particle is known, the range $x(E_{\text{kin}})$ can be extracted.

$$t_{\text{transit}}(x) = \int_{E_{\text{kin}}(x)}^{E_0} \frac{1}{v(E_{\text{kin}})\rho(x)S(E_{\text{kin}})} dE \quad (2.11)$$

As described in section 2.2, the different ranges in the target can be determined by varying the kinetic energy of the projectile.

It is not possible to measure the transit time of the primary protons directly but the prompt photons leave the target and the shape of their emission distribution is defined by the stopping kinematics of the protons. Therefore, a precise recording of this distribution can be used for range assessment.

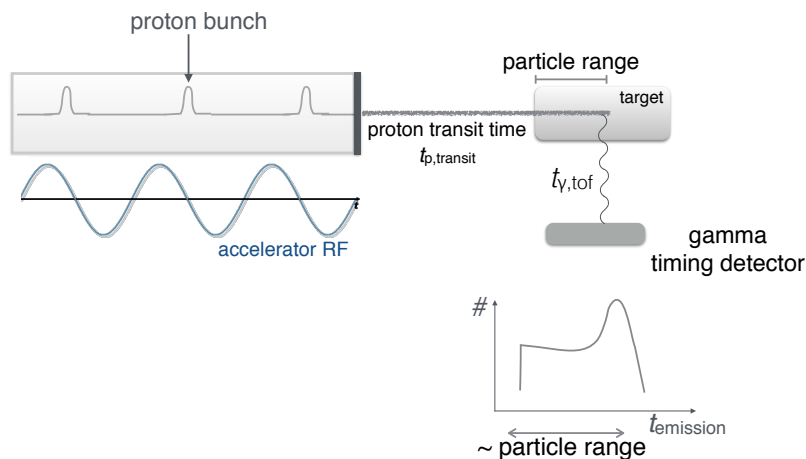


Figure 2.7: Scheme of the PGT method. A proton bunch exits the beamline and enters the target. Due to nuclear excitation of the nuclei, prompt photons are produced. The emission time distribution of these high energetic photons encode the range: a larger range is reflected in a longer period of prompt photon emission.

In practice, a common gamma ray detector measures the arrival time of prompt gamma rays related to the cyclotron radio frequency (RF). The RF as time reference is chosen because of the fixed phase relation with the bunch extraction. The recorded histogram ("PGT spectrum") includes the particle transit time through the material t_{transit} and the flight time of the corresponding prompt photons t_{TOF} . At higher incoming energies, the proton needs more time to cover the additional distance (longer range), and this leads to a longer emission period in the measured PGT spectra. Therefore, the prompt gamma timing peak is broadened and the center of the peak shifts, which indicates a longer penetration depth of the protons.

Of course, effects like the time resolution of the detector and the bunch spread smear out the spectrum. Nevertheless, considering the statistical momenta (e.g. the mean μ and the standard deviation σ) of the emission distribution, it is possible to extract a robust range information despite of the mentioned effects [15]. A detailed description of the PGT method can be found in C. Golnik et al. (2014) [15].

As briefly introduced in section 1.0.1, the measured PGT spectra are additionally influenced by the energy and time spread of the primary proton bunches as well as accelerator effects, like bunch phase fluctuations. To resolve these fluctuations, the time difference between scattered primary particles and a defined reference time must be determined. It is most convenient to measure the time against the accelerator RF because of the expected phase correlation to the beam bunches. However, if this correlation is unstable and changes, e.g. due to accelerator tuning, the prompt gamma profiles have to be corrected. Moreover, one can monitor the time and energy spread of primary protons by a bunch monitor. One possibility to extract the bunch structure parameters is to measure primary protons, which are elastically scattered at the exit window of the beam line or at a thin scatterer. The measured energy correlation and energy over time correlation spectra encode the structure parameters of the primary proton bunches and could be used for accurate reproduction of the PGT spectra.

2.4 Proton Accelerators

The proton bunch structure is mainly influenced by the operation of the accelerator. Nowadays, mainly two types of accelerators (synchrotrons and cyclotrons) for clinical proton therapy are commercially available. The presented experiments were mainly performed at the Cyclone 230 (C230)[®] cyclotron of the company Ion Beam Application (IBA). The working principle of this accelerator type is described in the following (figure 2.8).

Therapeutic cyclotrons are equipped with an ion source in their center, where hydrogen ions are produced by exploiting the chemi-ionization Penning effect. Free electrons are accelerated and ionize the hydrogen gas. Protons and other ions diffuse to a little hole in the source at the center of the cyclotron and will accelerate towards the nearest electrode. If they arrive at the right phase, they pass the selection system and will be further accelerated. For the acceleration a high frequency alternating voltage, which is applied between two hollow electrodes called "dees" because of their shape, is used. The dees are placed side by side with a narrow gap between them, where the protons are periodically accelerated. The particles are exposed to a magnetic field, which is perpendicular to the electrode plane and causes therefore the circular path of the particles.

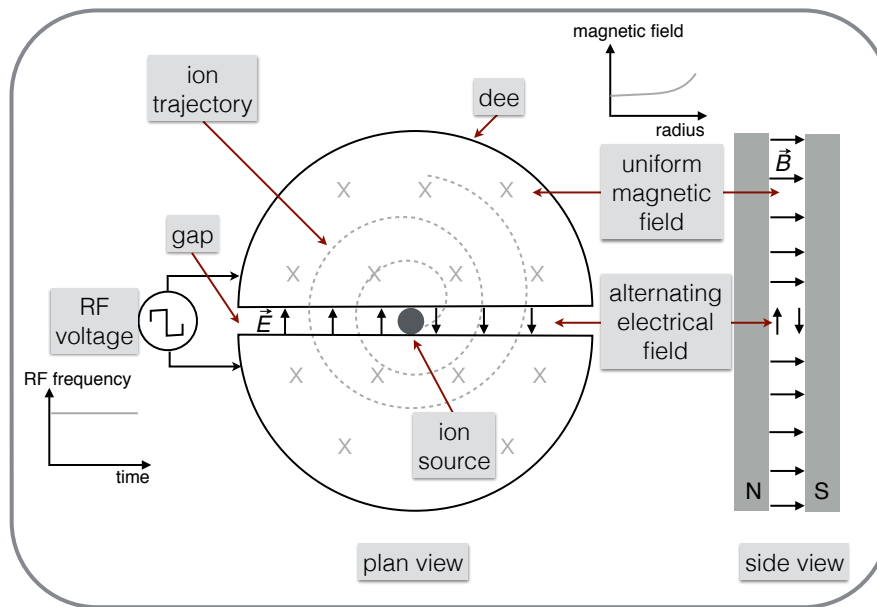


Figure 2.8: Cyclotrons use a magnetic field to cause particles to move in circular orbits. As the particles pass between the plates of the dees, the voltage across the gap is oscillated to accelerate them twice in each orbit. The accelerating field frequency is independent of the particle mass. To compensate the relativistic increasing of the particle mass at high energies, the magnetic field is raised at outer radii.

This typical circular orbit of radius r of charged particles (electric charge q) moving with the velocity $v = 2\pi r/T$ in the presence of a magnetic field B is due to the Lorentz force given in equation 2.12, which acts as a centripetal force.

$$F_{\text{Lorentz}} = \frac{mv^2}{r} = Bqv \quad (2.12)$$

According to equation 2.13, the period T of circulation does depend neither on the radius nor on the particle velocity, but on the magnetic field and the particle mass m .

$$T = \frac{2\pi m}{qB} \quad \Rightarrow \quad \text{frequency } f = \frac{1}{T} = \frac{Bq}{2\pi m} \quad (2.13)$$

If the magnetic field in the cyclotron is constant at each radius and the protons have the equal phase, they are at the same azimuthal angle.

To compensate the relativistic increase of the particle mass compared to its rest mass m_0 at high energies, the magnetic field is conventionally raised at outer radii. A measure of this relativistic effect is the Lorentz factor $\gamma = \frac{1}{\sqrt{1-v^2/c^2}}$, which leads to a mass increase of $\gamma = 1.24$ for protons with a kinetic energy of 230 MeV. Without the correction of the magnetic field (equation 2.14), the mass depending circulation time would change.

$$m(r) = \frac{1}{\sqrt{1-v(r)^2/c^2}} m_0 = \gamma(r) m_0 \quad B(r) = \gamma(r) B_0 \quad (2.14)$$

Consequently, the orbit frequency in a homogeneous magnetic field would drop with the energy and the protons would not longer be accelerated because of the lack of correlation to the RF. Nevertheless, a divergent magnetic field leads to an initial broadening of the proton bunch. To counteract this defocusing

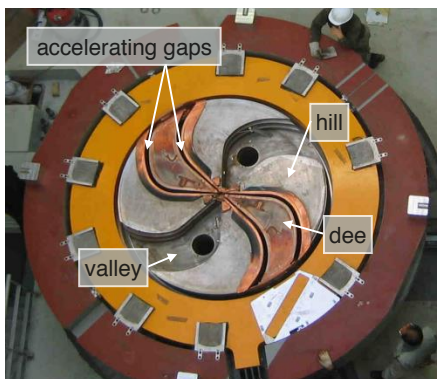


Figure 2.9: The C230 Cyclotron of the company IBA . Between the two dees the particles are accelerated. The hills (strong field) and the valleys (weak field) enable the vertical focusing, which is necessary because of relativistic effects [1].

IBA incorporated high and low magnetic field regions in the C230. The hills (strong field) and the valleys (weak field) enable the vertical focusing, which is necessary because of relativistic effects (figure 2.9).

Because of the narrow acceptance window in time and in the further acceleration parts, only a fraction of the protons leaving the source are actually being accelerated. At the IBA cyclotron the current of the beam at the source is adjusted by a feedback loop from the measured beam intensity.

The accelerator efficiency is additionally influenced by the extraction system, which is mainly responsible for the beam loss. If the extraction system works inadequately, it causes high radioactive components and enhanced wear and dirt deposition on insulators. The main challenge during particle extraction is to select protons from those that still have to make one or more turns and to ensure the beam structure during the extraction mechanism. The orbit radius of each proton increases with the momentum and approximately with \sqrt{E} . Therefore, a constant ΔE leads to a smaller orbit distance and a decreasing separation of the orbits near the extraction radius. In the IBA cyclotron, a self extraction system is included. The acceleration continues to a maximum possible radius, and the field is kept isochronous by using an elliptical pole gap, which is very narrow at the pole edge. The field drops to near zero in a short radial distance, so that the beam can be guided very quickly out of the main field through the fringe field. To get the extraction at a well-specified azimuthal angle, a groove in one hill is made near the extraction radius. A top-view of the cyclotron is shown in figure 2.9. The beam is deflected further by means of a septum and extraction cathode. To limit the beam size, several focusing elements are following the septum [1]. At the cyclotron exit, the proton bunch width is less than 1 ns.

For energy regulation, a degrader outside the cyclotron reduces the energy of the particles, depending on the desired water equivalent range. The protons undergo a certain number of collisions across the degrader material so that their velocity is reduced. Taking into account the statistical nature of this passive slowing down different protons end up with a slight energy difference known as energy straggling of the extracted bunch. The bunch width further increases as the bunch disperses through the beamline. The combination of the beam line acceptance ($\Delta E/E \sim 1\%$) and several momentum limiting slits allow to reduce the energy spread to a certain extent [1].

2.5 Scintillation Detector Principles

A scintillation detector, utilized to detect ionizing radiation, consists of a material, which converts the incident radiation into a flash of light. A coupled photomultiplier tube (PMT) transforms that amount of light into an electrical signal. The scintillation material of the detector should offer a high efficiency and, at best, a linear conversion of the kinetic energy of the incoming particle in visible or UV light. The emission of this light should be due to prompt fluorescence instead of the undesired contributions of phosphorescence, which has a larger wavelength and a much longer emission time. This means that the light yield, which defines the produced scintillation photons per deposited energy in the detector, should be proportional to the energy deposit over a wide energy range. Furthermore, the material should be transparent to its self emission spectra to ensure a maximal light collection. Additionally, the transition between the scintillation material and the photomultiplier or a photodiode has a higher coupling efficiency if the refraction indices are equal. In particular, in the case of fast following signal pulses, a fast decay time of the material is necessary to avoid pile up effects and to remain sensitive to consecutive signals in short time scales. The most widely applied scintillators are divided in two groups: the inorganic scintillators (e.g. sodium iodide) and the organic based liquid and plastic scintillators. Inorganic scintillators are characterized by a high light output and at the same time a linear conversion of the deposit energy. In contrast, scintillators based on organic materials have generally a better response time [16].

2.5.1 Organic Scintillators

The group of organic scintillators include crystals, liquids and polymeric solids. The scintillation mechanism is due to single molecule transitions in a higher energy level, independent of its physical state. The majority of the scintillation light in organic materials stems from the transition between the first higher single electronic state and the different vibrational ground states of the molecule. As shown in figure 2.10, the emitted light through de-excitation has almost always a lower threshold as the minimum energy required for transition in the nearest state and the material offers an efficient light collection, because it is transparent to the wavelength of its own emission spectrum.

In certain cases, an additional component in the scintillation material interacts as a wavelength-shifter. These additives absorb primary scintillation light and emit it at a longer wavelength. On the one hand, a possible self-absorption can be avoided. On the other hand, the emission spectra can be adapted to the coupled PMT.

The decay time of the most organic scintillators is in the range of nanoseconds and therefore relatively fast. The exponential course of the prompt fluorescence intensity depending on the decay time τ is given by:

$$I = I_0 e^{-t/\tau} \quad (2.15)$$

The response of organic scintillators to charged particles can be described by the Birks formula, which defines the fluorescent energy dL emitted per unit path length dx according to the specific energy loss dE/dx . The empirical relation 2.16 is non linear due to recombination and quenching effects (the quenching factor groups together all radiation-less de-exciting processes) between the excited molecules and the surrounding substrate.

$$\frac{dL}{dx} = L_0 \frac{dE/dx}{1 + k_B dE/dx} \quad (2.16)$$

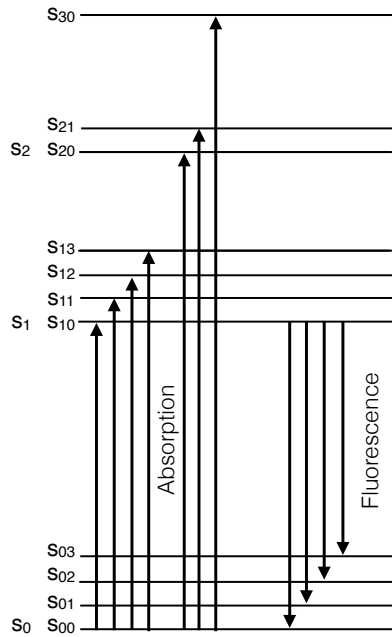


Figure 2.10: Energy levels of an organic molecule [16].

Here, L_0 is the light yield and k_B the Birks' constant, which depends on the material properties for a specific scintillator. For organic scintillators, the light yield for protons compared to electrons is generally smaller for equivalent energies and significantly nonlinear to much higher energies. Figure 2.11 shows that, at rising energies, the curves approach and the differences become smaller, but the response to protons is always below [16].

An important representative of organic scintillators are low-cost plastic scintillators, which can be produced in various forms like cylinders, rods or flat sheets at little effort. In first estimation the time response of a fast plastic scintillator can be described by a superposition of two exponential functions:

$$I = I_0(e^{-t/\tau} - e^{-t/\tau_1}) \quad (2.17)$$

One term describes the population of the levels from which the prompt fluorescence light arises. The other describes their decay, wherein the difference in the short rise time τ_1 and the longer decay time τ scales with a factor of five. The decay times of different plastic scintillators are typically in the range of 1 ns - 2 ns and are listed in table 2.1.

Table 2.1: Timing properties of fast plastic scintillators [16].

type	τ_1 (rise)	τ (decay)
NE 111	0.2 ns	1.7 ns
Naton 136	0.4 ns	1.6 ns
NE 102A	0.6 ns	2.4 ns

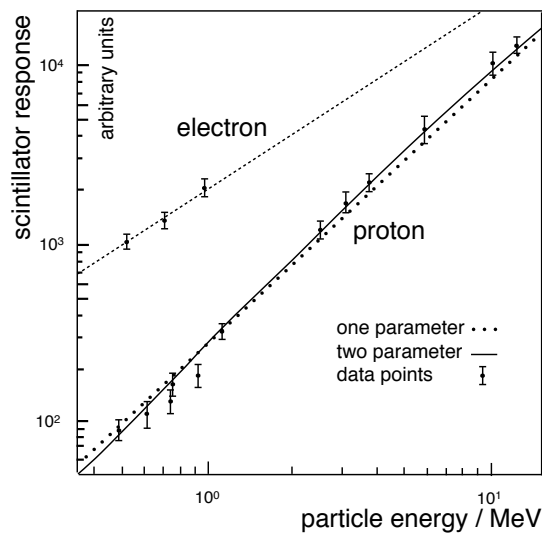


Figure 2.11: The scintillation response (ion-induced light output) for a NE 102 plastic scintillator. For organic scintillators, the response for protons compared to electrons is generally smaller for equivalent energies and significantly nonlinear to much higher energies [16].

2.5.2 Inorganic Scintillators

Inorganic scintillators are usually crystals doped with an additional component as activator. The crystal lattice determines the energy states of the electrons, wherein only discrete bands of energies are available. The electronic band structure model defines a valence band with electrons bound at lattice sites in the lowest energy state and a conduction band with free electrons, which can migrate throughout the crystal. In pure crystals, an intermediate band gap separates the electrons, and corresponds to the energy difference between the top of the valence band and the bottom of the conduction band. An excitation of a valence band electron into the conduction band with a subsequent return produces a photon with a wavelength above the visible range. To shift the wavelength of the emitting photons to longer wavelengths, the crystal are doped with amounts of an impurity called activators, which modify the band structure and creates intermediate states in the forbidden band. The energy difference for de-excitation from these recombination centers to the valence band results in a scintillation photon and determines the emission spectra of the scintillator.

If a charged particle enters the detection medium, it produces electron-hole pairs by transferring a part of its energy to an electron, which merges into the conduction band. Furthermore, the resulting defect electrons drift to recombination centers and ionizes them. Simultaneously, a free electron moves to such an ionized activator and re-combinates. The activator site remains in an excited state and returns to the ground state by emitting a photon with a wavelength in the visible range (figure 2.12).

Besides the recombination time of the electrons with the activators, which is very short, the time shape of the emitted scintillation light is mainly defined by the decay time (typically 30 - 300 ns) of the excited activators.

Compared to organic scintillators, the energy deposition is nearly proportional to the light yield, and the quenching effects are low and can be mostly neglected.

One example of a slow inorganic scintillation material is $\text{Bi}_4\text{Ge}_3\text{O}_{12}$ (BGO),

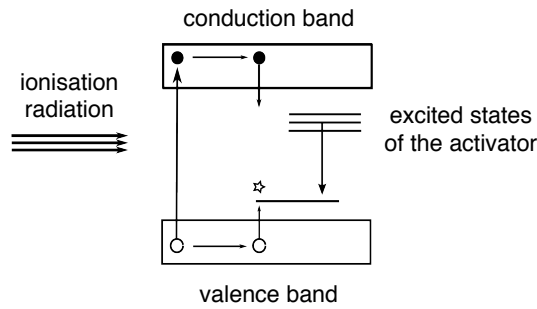


Figure 2.12: The mechanism of an inorganic scintillator [16].

which comprises bismuth, germanium and oxygen. Due to the high density of $\rho = 7.13 \text{ g/cm}^3$ and the large atomic number of the bismuth component ($Z = 83$), it has a large probability per unit volume for photoelectric absorption and is also suitable to stop high energetic charged particles to get a full energy deposition. Unlike sodium iodide (NaI(Tl)), it is non-hygroscopic and mechanically strong, and therefore widely applicable.

The decay time shown in figure 2.13, is a superposition of a 60 ns part, which represents 10% of the light yield, followed by a 300 ns component. In contrast to other inorganic crystals (e.g. lutetium oxyorthosilicate ($\text{Lu}_2(\text{SiO}_4)\text{O}$, LSO) $\tau_{\text{LSO}} = 47 \text{ ns}$ [16]), the timing resolution of BGO is substantially worse. A special feature of BGO is that no activator components are required, because the scintillation process is based on the transition of the Bi^{3+} -ion. The relatively large shift between the emission spectra and the absorption spectra is responsible for the high transparency over ranges of many centimeters. The emission (figure 2.14) starts at a wavelength of 350 nm (peak at 480 nm) and reaches beyond 600 nm [16]. The absorbed wavelengths are below 340 nm [17]. Nevertheless, the total detection yield of the scintillation light depends strongly on the purity of the crystal [16].

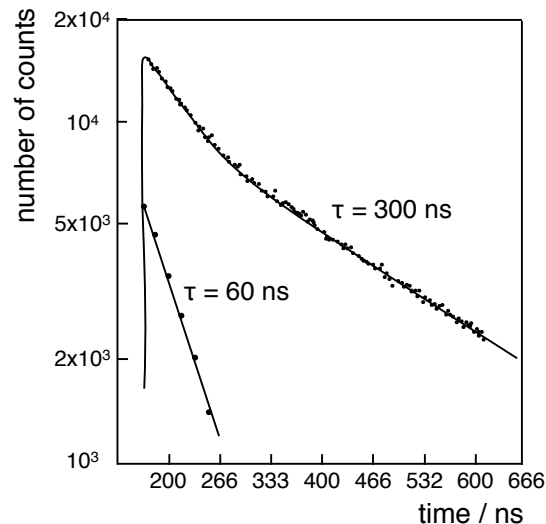


Figure 2.13: Measurements of the light pulse shapes from BGO. The abscissa represents time, the ordinate the relative light output. The BGO yield is represented as the sum of separate decay components with 60 and 300 ns decay times [16].

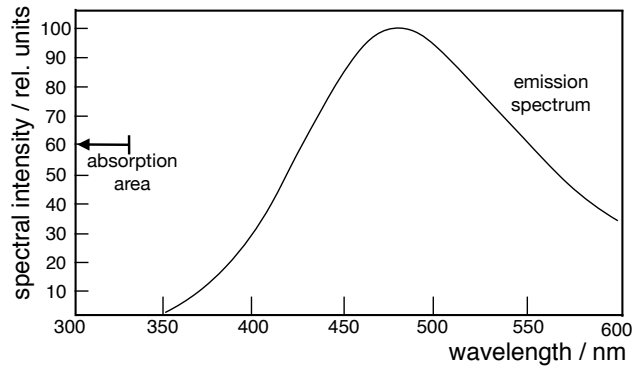


Figure 2.14: The emission spectrum of BGO. The relatively large shift between the emission spectra and the absorption spectra (below 340 nm) is responsible for the high transparency over ranges of many centimeters [16].

2.6 Phoswich Detector

A phoswich detector [18], [19] consists of two different scintillator materials stacked over each other and coupled with a single PMT. The pulse shape of the output signal depends on the two relative contributions of the used scintillator materials, caused by the different decay times [16]. Exemplary combination materials are CsI with GSO, BGO with GSO and plastic scintillators with BaF₂. Their decay times are listed in table 2.2. .

Table 2.2: Decay times of some scintillator materials [16].

	CsI(Tl)	GSO	BGO	plastic
Decay time	0.68 (64%)	0.056 (90%)	0.06 (10%)	~ 0.002
τ (μ s)	3.34 (36%)	0.4 (10%)	0.30 (90%)	

Due to their respective short and long decay time component, these detector construction can be used for particle identification. The shape of the output signal from the PMT depends on the relative contribution of the scintillation light from the two scintillators. Because of the differences in the produced pulse shape, particles can be distinguished by separating the electronic pulses from the fast and slow components of the PMT signal. This allows an independent measurement of the energy deposition in each scintillator without a second PMT.

As described in section 2.2.1, the energy deposition of a charged particle passing a slab of matter is described by the Bethe-Bloch formula and depends on the mass m and the squared electric charge z^2 of the incoming particle. Particles of different masses can be distinguished by a simultaneous measurement of the specific energy loss dE/dx and the residual energy E in the respective detector stages [16]. As referred in section 2.2.1 the specific energy loss scales with $1/v^2$, which is in first estimation proportional to m/E . In the energy correlation spectra (dE/dx as a function of the residual energy E) hyperboles are expected which are shifted along the ordinate because of the particle mass differences. Figure 2.15 shows that the curves, due to a decreasing particle mass, are closer to the abscissa.

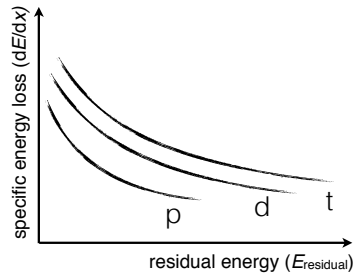


Figure 2.15: Scheme of an expected energy correlation spectra (dE/dx as a function of the total energy E) of a phoswich detector. The expected hyperboles corresponding to a decreasing particle mass are closer to the abscissa.

2.6.1 Pulse Timing Methods

For PGT application, it is important to precisely retrieve the arrival time of particles to the detector. Besides the acquisition electronics the timing signal depends on the detector properties. Effects, which influences the timing accuracy are divided in two groups. First, those which have a constant amplitude of the incoming signal but include random noise (time jitter) and second, uncertainties because of the variable amplitude of pulses (amplitude walk). The fluctuations in the signal pulse shape have different origins like electronic noise or the discrete character of the generated electronic signal.

As time pick off method in the later described experiments, a constant fraction discriminator (CFD) is applied, which produces an output signal if the leading edge of the pulse has reached a constant fraction of the peak pulse amplitude. This point is distinct for pulses with the same shape and different amplitude. Compared to other time trigger methods like leading edge triggering, wherein it is triggered at a fixed voltage value, CFD allows to accept pulses over a wide dynamic range (figure 2.16) [16].

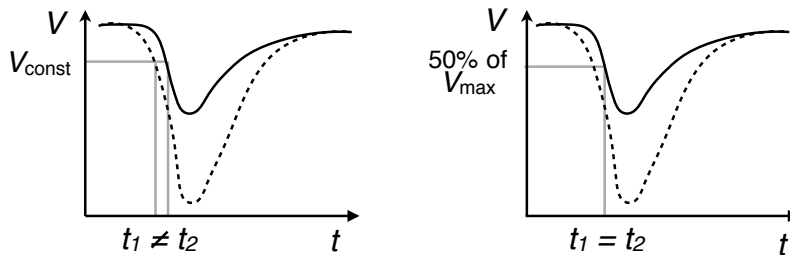


Figure 2.16: left: Illustration of the time "walk" seen for different signal amplitudes when using a leading edge discriminator with a fixed trigger point (V_{const}). right: The constant fraction discriminator (50% of V_{max}) showing how time walk is virtually eliminated for signals of different amplitudes.

2.6.2 Pulse Shape Discrimination

Besides the time of occurrence and the amplitude of detected events further analyzing methods offer opportunities to get additional information by analyzing the shape of the current signal delivered by the PMT. This temporal profile depends on the kind of particle. There are two common techniques for pulse shape discrimination (PSD): sensing the differences in the signal rise time or integration of the charge in two different time periods [16]. Figure 2.17 shows two pulses from different interactions. With the help of PSD, it is possible to distinguish between particles types in the detector by analyzing the deposited charge in the two gates. In the employed digital acquisition system the manufacturer incorporates an FPGA firmware for digital pulse processing - pulse shape discrimination (DPP-PSD). The fast contribution of the plastic scintillator (q_{short}) and the slow part of the BGO crystal (q_{long}) are integrated with two gates of different length. The individual duration of the gates can be set independently before starting the data acquisition.

Additionally, an online PSD cut (PSD_{cut}) processed by a FPGA can be set. This value is defined as $PSD_{\text{cut}} = \frac{q_{\text{long}} - q_{\text{short}}}{q_{\text{long}}}$ and allows an online cut of the events with higher/lower value, which reduces the data throughput significantly. Thus, the background can be discriminated, which generates a signal mainly in the plastic scintillator or in the BGO component, respectively.

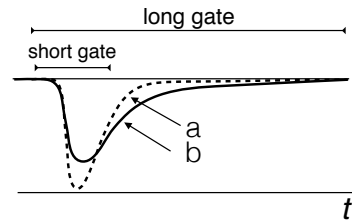


Figure 2.17: Two pulses from different particle interaction with different pulse shapes of particle type a and b.

Chapter 3

Concept

The treatment of patients is a certified process and requires a special procedure of experimental processes. In order to keep the implementation effort minimal, the intervention into the treatment process should be kept minimal. It is important that the treatment routine is not disturbed by additional measurements even if they increase their quality. This refers especially to the experimental setup concerning positioning (e.g. space for the detector or extra experimental components in the beamline) as well as the procedure of data acquisition and the design. The experimental setup for the acquisition of PGT data should be flexible, compact, and quickly positioned next to the patient table at little effort.

Because of the limited measuring time per applied fraction during a pencil beam treatment plan (one layer correlated to a fixed energy lasts a fraction of a second [20]), a further challenge is to ensure the required statistic to get a robust estimation of the desired structure parameters from the recorded data. The application of an experimental system, which is based on digital data acquisition, could allow to fulfill these requirements and is therefore investigated. The present setup is intended for experiments under clinical conditions, e.g. parasitic measurements during quality assurance.

3.1 Digital Pulse Processing

One possible alternative to analog pulse shaping techniques, which are often quite hardware-complex and expensive, is the digital processing of pulses. Nowadays, the ongoing development in high speed analog-to-digital converter (ADC) provides a more precise conversion of an analog pulse from a detector signal into a sequence of digital samples along the pulse. Present ADCs deliver a long sequence of samples with sampling rates in the range of several hundred mega samples per second as well as high processing rates. This ensures a high granularity of the recorded waveform in the range of nano seconds. In order to apply pulse shaping to a signal it is an advantage to be able to set the shaping parameters during run time. These can be easily changed for shaping or filtering the pulse, which encodes the pulse information as a digital string of numbers, by basic mathematic operations. In opposition to analog processing the subsequent processing of digitalized data is less complex in terms of hardware.

If a fast timing information is important, digital systems are in principle limited in timing accuracy to the nearest period of the samples points. A high sampling frequency allows a more precise determination of the pulse timestamp [16]. In order to increase the timing resolution a special software algorithm

can be used for analyzing the recorded pulse shape. One possibility (CFD-triggering) is described in section 2.6.1.

The most critical and complicated step in digital data acquisition is to convert the analog signal in discrete data samples, by receiving the waveform of the incoming signal as well as possible.

Each value of a data sample is proportional to a differential input voltage and is read out by a fixed clock frequency in constant intervals. In the later described experimental setup, a 12 bit digitizer with a maximum sampling rate of 250 MS/s transfers the analog waveform in sample points with a distance of 4 ns in a co-domain of 4096 voltage values [21]. In the last experiment a 14 bit digitizer with a sampling rate of 500 MS/s was used.

To extract the nature of the detected event including the particle type, analysis of the detailed shape and the time profile is necessary. In any case, this is always a compromise between the complexity and the performance of the analyzing algorithm, caused by real time analysis at high counting rates, which is limited through the time between the signal pulses.

In the case of very fast consecutive pulses, it is in principle possible to include pile up events through the analysis of the pulse shape by separating the different components of the superposed signals. Nevertheless, the processing time of this pile up analysis is quite long and not a standard routine in spectroscopy systems, where the pulse analysis is carried out in real time.

The sample points between the pulses are used for baseline restoration [16]. The firmware algorithm of the digitizer calculates continuously the baseline inside a moving window from a fixed number of points, which can be set in the software. The difference between the baseline and the input signal is compared with the trigger threshold. If there is a surpass it is triggered. The baseline is then frozen to the end of the maximum value between the start of the integration gate (long gate, short gate) and the trigger hold off. After that, the baseline restarts again its calculations. The main parameter which can be set in the software directly before the data acquisition are shown in figure 3.1 [21].

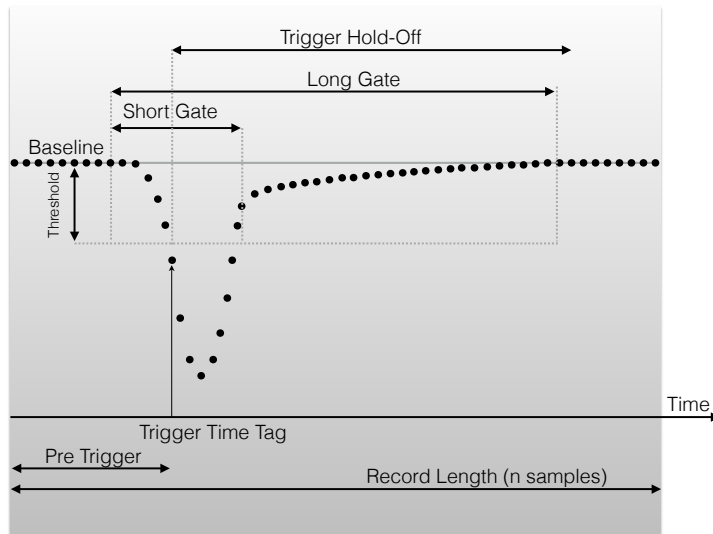


Figure 3.1: Illustration of a sampled waveform with the most important software parameters for one acquisition window.

3.2 Materials and Methods

The current experimental setup for a bunch monitoring system is shown in figure 3.2 and consists of a CAEN desktop digitizer (DT5720/DT5730), a self-built phoswich detector, a CAEN high voltage (HV) module DT5330 and a compact computer.

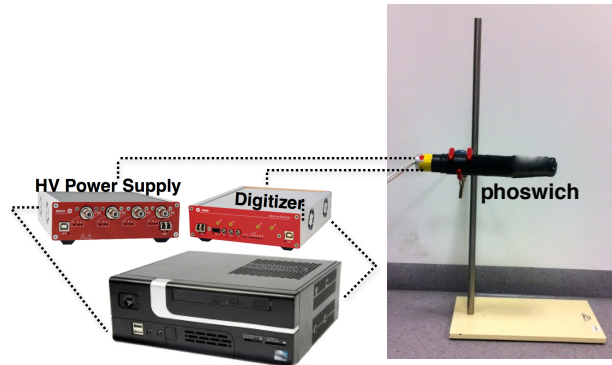


Figure 3.2: The experimental setup of a phase bunch monitor system: The phoswich detector is connected to a CAEN Digitizer, which records the waveform of the incoming signal and transfers the digital list mode data to the computer. The CAEN HV-module DT5330 supplies the photomultiplier tube (Photonis XP2972) of the detector.

The detector, deployed for proton scattering experiments, has a dimension of approximately 6 cm x 3 cm x 3 cm (frustum) and comprises a 9.5 mm long fast plastic scintillator (PVT-based) to get a good timing resolution and a 5 cm thick BGO crystal, with a high density of $\rho = 7,13 \text{ g/cm}^3$ for energy deposition (figure 3.3). Due to the fast contribution of the plastic scintillator (decay time: $\tau < 10 \text{ ns}$ [16]) and the slow part of the BGO signal (decay time: $\tau \approx 300 \text{ ns}$ [16]) results in an individual pulse shape for the distinct particles. Therefore, particle identification by means of a pulse shape discrimination algorithm is possible.

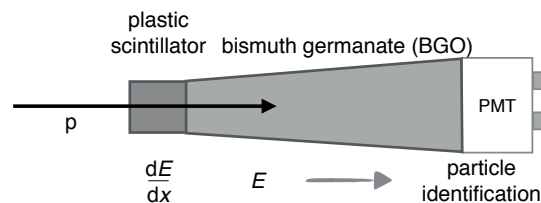


Figure 3.3: The phoswich detector for charged particle identification consists of a fast plastic scintillator to get a good timing resolution and energy loss rate (dE/dx). A BGO crystal measures the full energy deposition E_{residual} of the particle.

The individual length of the respective integration gates should be adapted to the decay time of the scintillation materials. As referred in section 2.5, the scintillation emission depending on the decay time can be described by an exponential function. To integrate 86.47% of the area the related gate length needs to be in the range of 600 ns (BGO) and 20 ns (plastic scintillator). These

values have to be converted in sample points n depending on the sampling rate (e.g. sampling rate of 250 MS/s with 1 sample $\hat{=} 4$ ns: $n_{\text{BGO}} = 150$, $n_{\text{plastic}} = 5$). The signal output (PMT - Photonis XP2972) of the phoswich detector is connected to a desktop CAEN digitizer (50 Ω) with a maximum sampling rate of 250 MS/s (DT5720) and 500 MS/s (DT5730), respectively. The waveform can be recorded deadtimeless. The tools available for processing and analyzing the input signal include:

- continuous conversion of the input signal into digital samples with an external/internal trigger
- setting two independent integration gates with different widths and position for PSD
- baseline calculations including subtraction of the incoming signal
- generate output files including the integrated charge values of the long and short waveform part, the trigger time stamp and the sampled waveform for other spectroscopy analysis software tools

The digitizer provides three different acquisition modes for an online PSD: the oscilloscope mode, list mode and mixed mode. The mixed mode offers the possibility to transfer the charge and time stamp information as well as samples of the raw waveform. Besides the internal clock, where the digitizer samples with its maximum sampling rate, an input connector for an external clock as reference allows a straight correlation of the signal with the accelerator frequency and generates the rough trigger time stamp (e.g. sampling rates: 106 MS/s, 212 MS/s, 424 MS/s). Besides the trigger time stamp a more precise arrival time of the protons in the detector is determined by an offline constant fraction algorithm. To implement the constant fraction timing in the experimental data acquisition, the digitizer transfers a sufficient amount of sample points of the raw waveform in a special region of interest, so that a reasonable throughput bandwidth is kept. Additionally, the signal is smoothed by a moving average filter with a fixed sample width to reduce the noise. An interpolation of the waveform samples around a fraction of the amplitude increases thereby the timestamp generation precision. Figure 3.4 shows a superposition of recorded waveforms of the phoswich detector and depicts the length of the two integration gates.

As mentioned in section 3.1, the firmware algorithm continuously calculates the baseline of the input signal, compares it with the value of the trigger threshold and the trigger fires as soon as the signal crosses the threshold. If the trigger fires, the signal is delayed by a programmable number of samples (pre-trigger). In this way the gates for charge integration can start before the trigger (gate offset value). The baseline remains frozen to the last averaged value and its value is used as charge integration reference. During the whole duration of a programmable “trigger hold-off” value, other trigger signals are inhibited. The trigger enables the event building, that includes the waveforms (i.e. the raw samples) of the input, the trigger time stamp, the baseline, and the charge integrated within the gates. The event data is saved into a memory buffer and becomes immediately available for the readout.

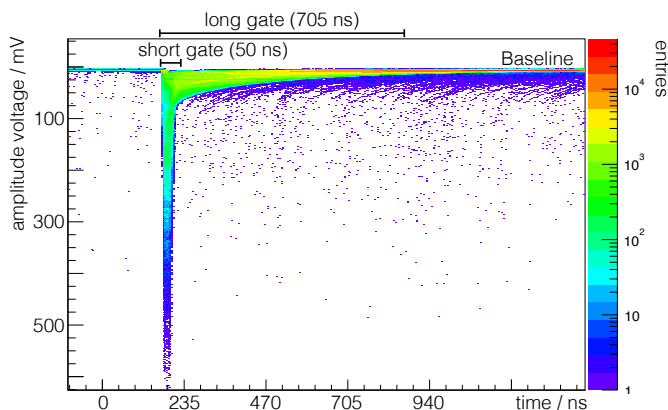


Figure 3.4: Superposition of recorded waveforms of the phoswich detector with sample points in a distance of 4.7 ns (sampling rate: $2 \times 106 \text{ MHz} \rightarrow 212 \text{ MS/s}$) produced by scattered protons. The pulse shape discrimination algorithm interprets the waveforms through two independent charge integration gates - the short gate for the plastic scintillator and the long gate for the BGO crystal.

A DPP-PSD firmware update of the DT5730 digitizer, which was available in the last experiment, provides the possibility to perform an online CFD processed by a FPGA. After the implementation it is not longer necessary to transfer parts of the raw waveform, which increases the data throughput. A scheme of the working principle is shown in figure 3.5.

The input signal is split and simultaneously modified in two different ways. One path is responsible for the attenuation of the signal. Possible values, which reduces the signal to a fixed fraction of the maximum input amplitude, are 25%, 50%, 75% and 100%. This values define the desired timing fraction f of the full amplitude.

The other part delays and inverts the signal through a FIFO (first-in first-out). The delay time d is the time to reach the maximum amplitude from the CFD level and can additionally be set in the software.

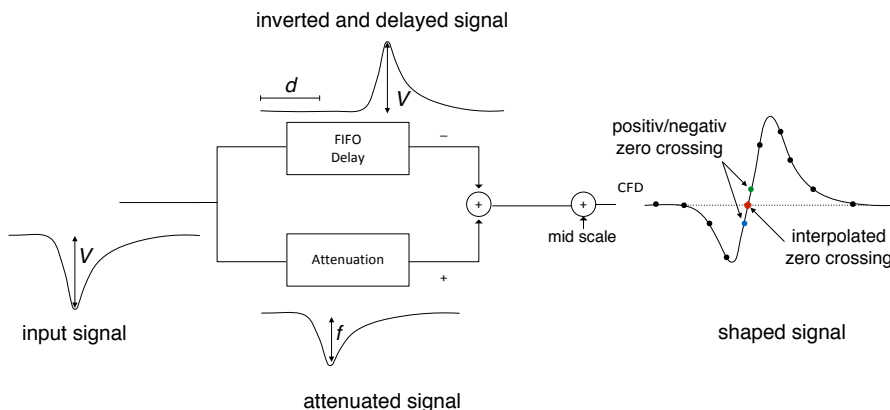


Figure 3.5: Scheme of the operating principle of the digital CFD in the DPP-PSD firmware update of the CAEN DT5730 digitizer. After modifying the input signal in two different paths the more precise time stamp is generated by an interpolation around the zero crossing [21].

After the modification of the input signal, the two parts of the waveform are superposed and the zero crossing algorithm can be applied. The more precise time stamp of the resulting signal is determined by an interpolation of the samples before and after the zero crossing (fixed midscale of the dynamics).

As referred in section 2.6.2 a PSD-cut can be set to online discriminate a part of the background. Figure 3.6 ($PSD_{\text{cut}} = 0.12$) and figure 3.7 ($PSD_{\text{cut}} = 0.9$) show two energy correlation spectra with the respective energy cuts.

For timing measurements a reference signal must be determined. In the following presented experiments the accelerator RF (106 MHz) is used for synchronization of the digitizer which has an AC coupled differential input port. This allows a straight correlation of the signal with the pulsed proton bunches extracted from the cyclotron ($2 \times 106 \text{ MHz} \rightarrow 212 \text{ MS/s}$).

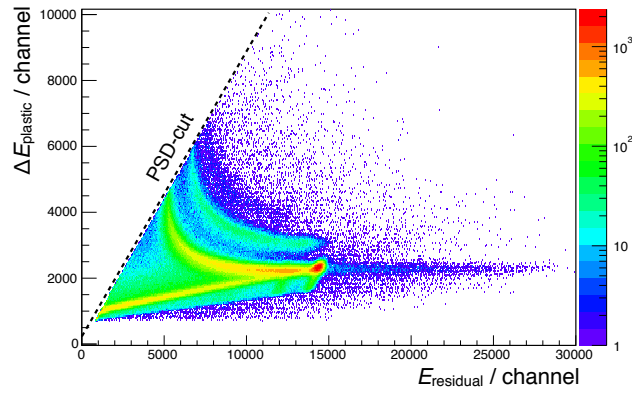


Figure 3.6: Energy correlation spectra with an online energy cut of $PSD_{\text{cut}} = 0.12$.

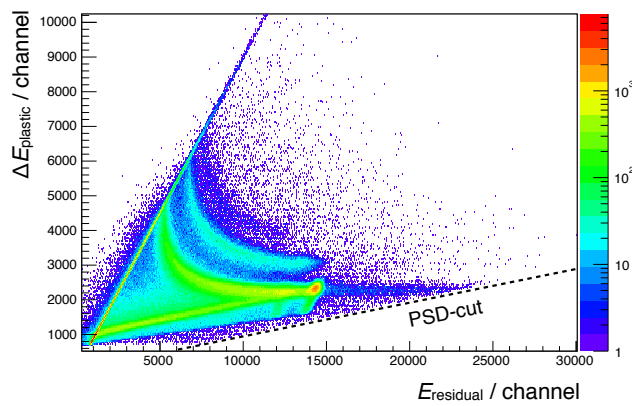


Figure 3.7: Energy correlation spectra with an online energy cut of $PSD_{\text{cut}} = 0.9$.

3.3 Bunch Monitoring

As mentioned in section 2 bunch time and energy width of the proton bunches depend on the kinetic energy of the particles as well as on the accelerator parameters and varies during beam tuning. Even in clinical applications, it exists neither an independent control system nor any reference values concerning the beam micro structure. In the following one possible procedure which allows to monitor these parameters is described.

During the irradiation with high energetic charged particles a high background occurs due to several interactions with the target material. This includes, as referred in section 2.2, atomic excitations which causes mainly the low-energy background and nuclear interaction which leads to the production of secondary particles (deuterons, alphas and neutrons) in addition to high-energy photons and positron emitters.

Figure 3.8 (A) shows a typical energy correlation spectra (PSD plot) of a scattering experiment with protons (kinetic energy $E_{\text{kin}} = 220$ MeV) recorded with a phoswich detector. The y-axis represents the specific energy loss $\Delta E_{\text{plastic}}$ and the x-axis the total deposited energy E_{residual} measured in the related detector stages. The distinct particle hyperboles in the spectrum confirm the assumption in section 2.6.

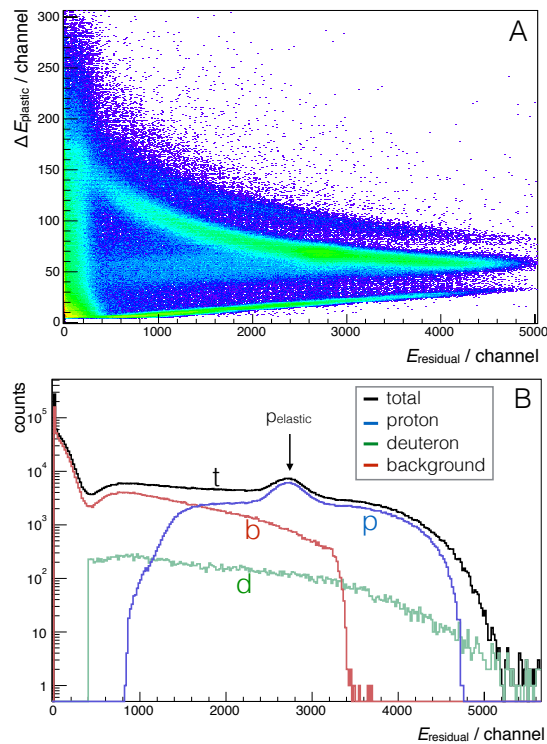


Figure 3.8: A: A typical energy correlation spectra of a scattering experiment with protons (kinetic energy $E_{\text{kin}} = 220$ MeV) recorded with a phoswich detector. The distinct lines in the spectrum indicate different particles. B: Phoswich detector combined with pulse shape discrimination firmware allows particle identification and background discrimination. The elastically scattered protons occur as a peak.

Besides the scattered protons other particles like deuteron, neutrons and gammas are detected, which can be separated due to the detector properties. Figure 3.8 (B) shows a 1D histogram of the residual energy for the distinguished

particles, in which the elastically scattered protons occur as a peak. The energy cuts for E_{residual} and $\Delta E_{\text{plastic}}$ have been set to fixed intervals for the respective curves.

Furthermore, in the two dimensional energy correlation spectrum the protons can be isolated through an energy cut following a hyperbolic function (figure 3.9 (A)) by defining an upper and lower energy limit. The elastic scattering peak, which becomes visible after decomposition, encodes the primary particles bunch structure and the respective bunch widths $\sigma_{\text{monitor}}^2 = \sigma_{\text{Bunch}}^2 + \sigma_{\text{detector}}^2$ can be extracted. For example, figure 3.9 (right) shows the 1D projection of the residual energy (B) and the 1D projection of the detector arrival time with respect to the accelerator RF (C). Thus, the respected bunch widths of the primary proton bunch can be extracted from the distribution of the scattered protons.

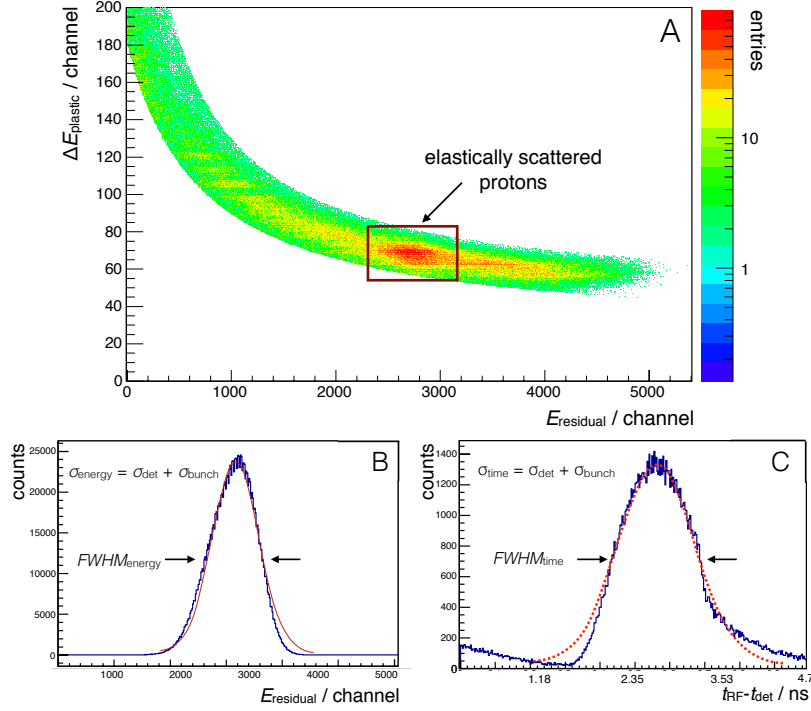


Figure 3.9: A: Scattered protons isolated through an energy cut following a hyperbolic function by defining an upper and lower energy limit. The elastic scattering peak (red area), which comes out after decomposition, encodes the primary particles bunch structure. B,C: The projection of the residual energy of the elastically scattered protons allows a exclusion of the respective bunch widths.

For experiments in the experimental hall, it is possible to place scattering materials directly in front of the exit window of the beamline (figure 3.10). If the proton beam passes a thin foil some protons are scattered and can be detected. It is important that neither the scattered protons nor the primary protons undergo a significant spread of the time and energy bunch widths. This means that the target has to be as small as possible while ensuring the required statistic of scattered protons.

The scattering angle, at which the bunch monitor is placed, defines for the scattered protons their residual kinetic energy. As shown in figure 3.10 the experimental setup allows to monitor the bunch structure parameters without disturbing PGT measurements.

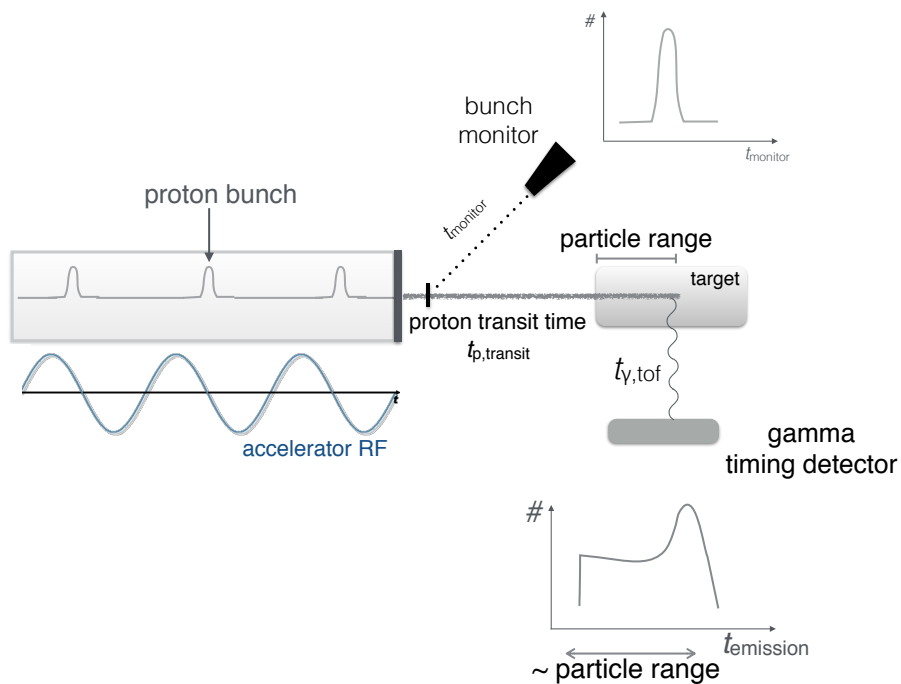


Figure 3.10: A thin foil in front of the exit window serves as scattering body, while receiving the bunch structure of the primary protons. The bunch monitor measures at a defined angle the time and energy distribution of the elastically scattered protons without disturbing PGT measurements. From the recorded spectra the respective bunch structure parameters can be extracted and used for corrections in PGT measurements.

Chapter 4

Experiments and Results

The first scattering experiments of high-energetic charged particle beams using the bunch monitor setup have been performed at Helmholtzzentrum für Schwerionenforschung (GSI) Darmstadt, Helmholtz-Zentrum Dresden-Rossendorf (HZDR) and OncoRay, Dresden. These experiments include the evaluation of the timing and energy structure of particle beams as well as the first experiments to estimate the detection yield. Additionally, the energy straggling of the bunch due to the length of the beamline was investigated and an estimation of the detector time resolution were carried out. The different experiments are performed as follows:

- A Schwerionensynchrotron (SIS18) at GSI: scattering experiments with ^{12}C -ions ($E = 200 \text{ AMeV}$) for first energy measurements with a phoswich detector.
- B Electron Linac for beams with high Brilliance and low Emittance (ELBE) linear accelerator at HZDR: experiments with bremsstrahlung photons for first timing measurements (evaluation of the offline CFD) with a sodium iodide detector.
- C Cyclone 230 (C230) cyclotron at OncoRay: experiments at a clinical proton beam with a phoswich detector.
 - (a) Scattering experiments to attempt an energy calibration and time of flight measurements for particle identification.
 - (b) Scattering experiments with thin foils of various materials to estimate the detection yield.
 - (c) Scattering experiments with a thin aluminum foil to estimate the energy straggling due to the length of the beamline and to extract the detector timing resolution (evaluation of the online CFD).

4.1 Preparatory Experiments

The experiments at the SIS18 synchrotron (section 4.1.1) and the ELBE linear accelerator (section 4.1.2) were performed for a basic commissioning of the digital data acquisition system. This includes the determination of various parameters, which can be set in the control software, and the evaluation of the acquisition software itself.

The standard operation software of the digitizer provided by the manufacturer CAEN can be only used in the oscilloscope mode of the digitizer.

In this mode the input signal is shown and one can adjust the parameters for the acquisition but special features are absent (e.g. transfer parts of the waveform). According to the desired application, the digitizer operates in the mixed mode. Consequently, an own software had to be developed and complemented.

4.1.1 SIS18 Synchrotron at GSI Darmstadt

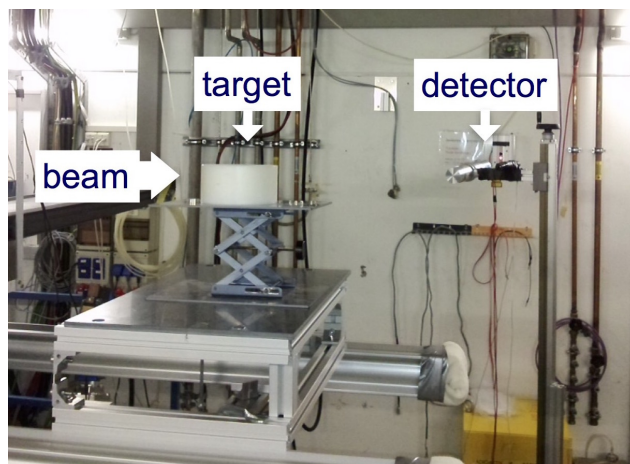


Figure 4.1: Picture of the experimental setup at GSI. The ^{12}C -ions were extracted from a horizontal beamline and enter a PE target. The detector was placed at a distance of 115 cm at an angle of 66° .

At GSI Darmstadt, first energy measurements of secondary protons at the synchrotron SIS18 were conducted. As shown in figure 4.1, a 10 cm x 30 cm x 30 cm polyethylene (PE) target was irradiated with ^{12}C -ions of an energy $E = 200 \text{ AMeV}$. The detector was placed at a distance of $d = 115 \text{ cm}$ and an angle of $\alpha = 66^\circ$ relative to the beam axis. The measurements were carried out as parasitic experiments during beam tuning. In the experimental cave, only energy measurements of the scattered particles were possible, because a time reference like the RF of the accelerator was not available.

As introduced in section 2.6.2, for energy measurements, the DPP-PSD firmware distinguishes between a long integration gate for the total detector deposition energy E_{residual} , which encloses the BGO component of the waveform, and a short gate, which associates to the plastic scintillator and defines the specific energy loss $\Delta E_{\text{plastic}}$ in it.

The recorded energy correlation spectrum is shown in figure 4.2. In the spectrum an offline PSD-cut was applied to discriminate a part of the background (particles, which deposit their energy mainly in a single detector stage). As expected from previously published measurements [6], the spectrum shows two separated curves: a typical proton line and a deuteron line, which results from inelastic nuclear reactions (e.g. fragmentation, pick up reactions).

Because of the limited length ($l = 5$ cm) of the BGO crystal, which is responsible for the full energy absorption and therefore the stopping of the particles, only protons with an energy of up to ~ 170 MeV can deposit their entire energy [8]. This restriction leads to a buckling in the energy line (seen at channel $E_{\text{residual}}(5700, 7100)$ and $\Delta E_{\text{plastic}}(1400, 1900)$).

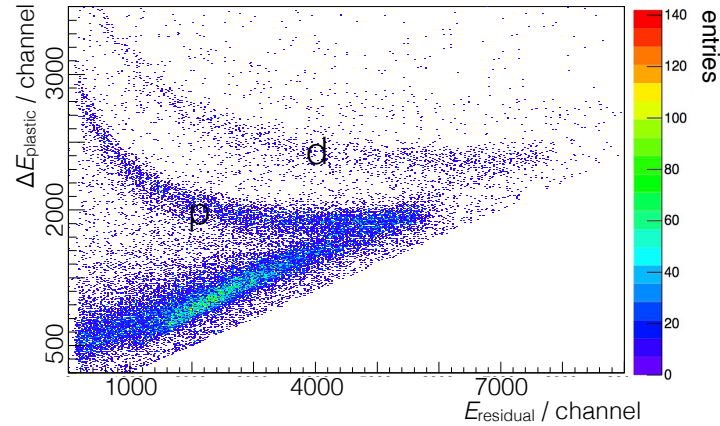


Figure 4.2: Correlation of energy loss and residual energy measured at GSI. The phoswich detector allows the separation of hydrogen ions and deuteron ions. Calibration of channels to energy by means of elastically scattering peaks was not possible, as the BGO was not thick enough to stop the protons completely.

The first task was to measure the deposited energy in the respective detector stages of the phoswich detector. Unfortunately, the accelerator parameters changes between the different experiments because of the beam tuning procedure and it was not possible to get the detailed beam settings. As referred a time reference signal was not available so that the digitizer was internally clocked (sampling rate of 250 MS/s).

Before energy integration, the input signal was smoothed with a moving average filter. The integration gates had a length of 6 samples (24 ns) for the short part (specific energy loss dE/dx in the plastic scintillator) and 220 (880 ns) samples for the long part (residual energy in the BGO crystal) of the recorded waveform.

The spectra in figure 4.2 show that it was possible to measure the residual energy of the scattered protons with a simultaneous separation of secondary particles.

4.1.2 ELBE Linear Accelerator at HZDR

At the ELBE accelerator (HZDR), a sodium iodide scintillator detected bremsstrahlung photons (up to 12.5 MeV) produced by a 13 MeV electron beam hitting a niobium foil (figure 4.3) to investigate the timing capabilities. The accelerator is very well suited for timing measurements because of the low time jitter of less than 50 ps [22]. The electron current was less than $1 \mu\text{A}$.

In the experiment, the accelerator RF (13 MHz) was used as time reference

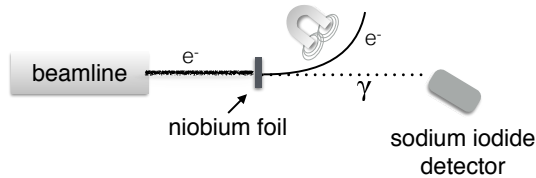


Figure 4.3: Experimental setup at the ELBE accelerator.

and was sampled by an additional channel of the digitizer. This was the first test where the detector time was measured with respect to a reference signal, namely by determining the zero crossing of each RF pulse. As detector time stamp, an offline constant fraction timing was tested to get a more precise arrival time of the photons in the detector with respect to the RF.

The energy over time correlation spectrum of the photons is shown in figure 4.4 a. At low energies the spectrum is smeared out. One reason therefore are time walk effects (section 2.6.1). The CFD trigger minimizes this effect, but cannot compensate it completely (especially at low energies and small pulse amplitudes). Figure 4.4 b shows the projection of the obtained time spectrum. The measured detector time resolution without a specific energy cut for the incoming photon bunches was 1.7 ns full width at half maximum (*FWHM*). Because of the long decay time $\tau_{\text{NaI(Tl)}} \sim 250 \text{ ns}$ the detector is actually not suitable for timing measurements, but it performs sufficient well to show the feasibility of the CFD algorithm on this hardware on a wide dynamic range.

The uniform horizontal pattern in the spectra is due to a ^{60}Co source, which

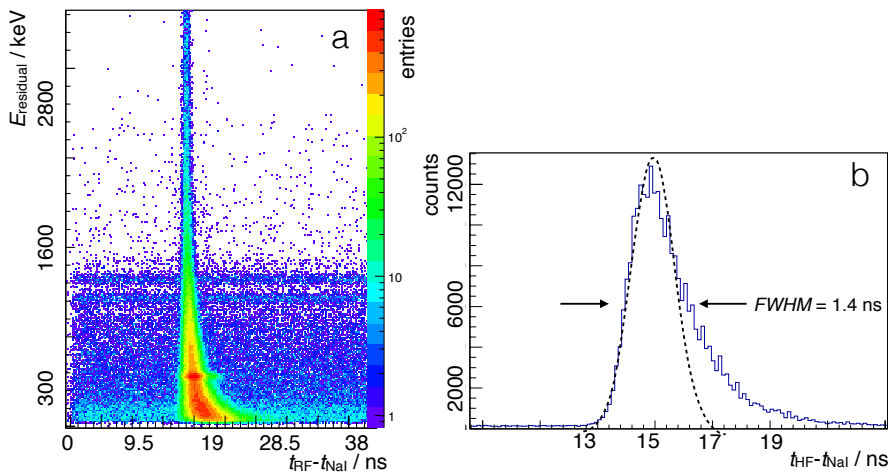


Figure 4.4: a) Energy deposition (E_{residual}) over time correlation spectrum with respect to the accelerator RF ($t_{\text{RF}} - t_{\text{NaI}}$) measured at ELBE (HZDR). b) Projection of the reference time spectrum, revealing a $FWHM_{\text{time}}$ of 1.7 ns.

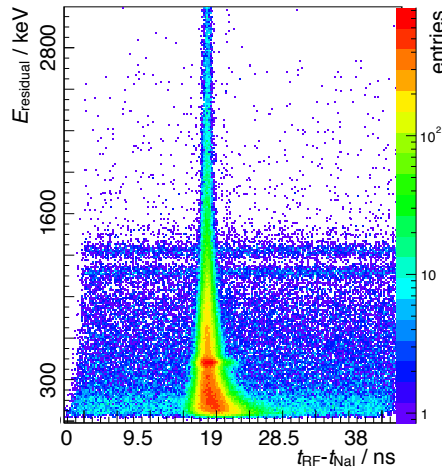


Figure 4.5: The recorded spectrum at ELBE (figure 4.4) after applying a time walk correction. The remaining smearing at low energies is due to a low statistic of scintillation photons while considering a wide dynamic range.

was placed close to the detector. The corresponding 1173 keV and 1332 keV photons are uncorrelated to the RF and a distinct line across the time axis arises. The peak at low energies are due to 511 keV pair production photons. The prolongation towards later times might be a result from the finite positron life time.

Unlike the experiment at GSI, first time reference measurements were possible. Time walk effects influences the spectrum, which is shown in figure 4.4. After applying an algorithm to compensate the time walk [23] the corrected spectrum (figure 4.5) has a lower distortion.

For these corrections, the mean time of the peak centroid t_m for different energy slices of the recorded spectra is determined. The resulting values fitted by an empirical function are shown in figure 4.6. The fit function with E_0 , t_0 and t_s as free fit parameters is given by:

$$t_m = t_s \exp(-\sqrt{E/E_0} + t_0) \quad (4.1)$$

and the resulting function for the corrected time t_c by:

$$t_c = t - t_s \exp(-\sqrt{E/E_0}) \quad (4.2)$$

A more detailed description of the algorithm can be found in *Hueso-González et al.* (2014) [23].

Besides this, the smearing at lower energies cannot be compensated through the algorithm as it is due to a low statistic of the scintillation photons. Because of the wide dynamic range the supply voltage at the PMT was $U = 600$ V. Especially low energy photons produce only a few scintillation photons, which causes higher uncertainties (relative error: $\Delta N/N \propto 1/\sqrt{N}$) and therefore an inaccuracy of the time stamp.

This effect can be observed in figure 4.7, which shows the measured time width for different energy slices. The extracted $FWHM_{\text{time}}$ increases significantly with low energies (\propto low channels) from 0.6 ns to 2.9 ns.

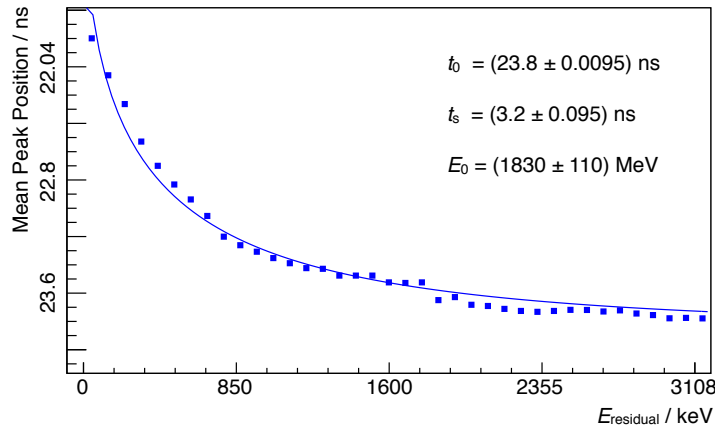


Figure 4.6: The determined mean peak positions of the measured photon arrival time as a function of the photon energy. The experimental data is fitted with the empirical function 4.1.

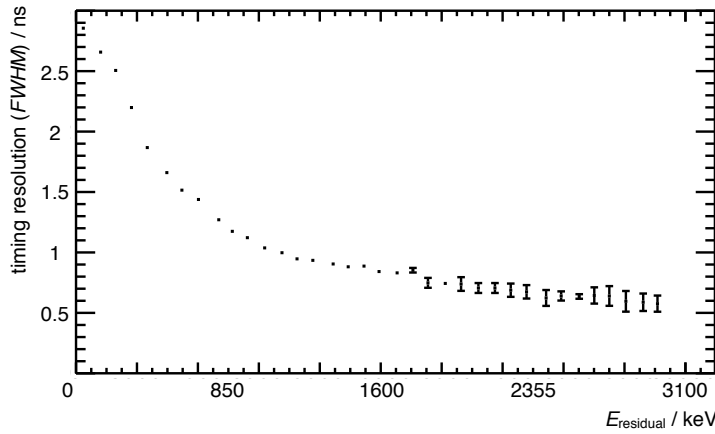


Figure 4.7: The time width of bremsstrahlung photons measured at ELBE decreases significantly with higher energies.

In these two preparatory experiments, the digital system was employed for the first time to measure scattered particles. By recording first energy correlation and energy over time spectra, it was possible to gain first experiences according to handling and positioning of the experimental setup. Additionally, the control software could be tested and a first value range for important software parameters could be determined. The time reference measurements allowed a first applying of the offline CFD algorithm, wherein the digitizer was synchronized with the accelerator frequency.

4.2 C230 Cyclotron at OncoRay Dresden

Having demonstrated that the experimental setup is capable of measuring the energy and the time correlation spectra of different scattered particles, further experiments focus at implementations at the OncoRay facility in Dresden, where a clinical proton beam is available for additional investigations.

The Cyclone 230 (C230) [®] of the company Ion Beam Applications (IBA) delivers protons to an experimental room (fixed horizontal beam) and a treatment room (gantry). Compared to classical research cyclotrons of the same max. energy, the C230 has a compact design with a diameter of 4.2 m and a weight of 220 t [24].

The beam delivery system produces a continuous fixed energy (230 MeV) proton beam with a maximum beam current of 300 nA and a fixed accelerator frequency of 106 MHz. A central ion source delivers protons by ionizing hydrogen gas. After leaving the ion source, the emitted protons are subjected to a high magnetic field (2.2 T), which confines the protons into a spiral shaped orbit. Meanwhile, they are periodically accelerated in four gaps by a RF system, which provides a strong electric field due to two electrodes ("dees"). The dee voltage oscillates between 55 kV and 150 kV. If the protons reach their maximum energy, the extraction system guides the particles into the beam transport system. Afterwards, the protons were passively slowed down to the requested kinetic energy (see section 2.4).

4.2.1 Energy Calibration and Particle Identification

Energy Calibration

The first experiments at a clinical proton beam at the OncoRay facility cover the calibration of the phoswich detector. Due to the high kinetic energy of particles in several experiments and the limited size of the absorption crystal it is not possible to perform an energy calibration by means of the elastically scattered proton peaks in each experiment. Hence, it is necessary to examine if the established energy calibration can be used in further experiments with high-energetic protons.

In first experiments protons were scattered on a thin target ($d=1$ mm) consisting of polyethylene (C_2H_4) and detected at an angle of $\alpha = 40^\circ$ (figure 4.8). The requested current at the cyclotron was $I(217 \text{ MeV}) = 4 \text{ nA}$ and $I(106 \text{ MeV}) = 50 \text{ nA}$. The data acquisition lasts in each setup five minutes.

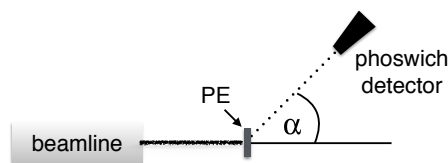


Figure 4.8: Scheme of the experimental setup of first scattering experiments. Protons were scattered on a thin target ($d=1$ mm) consisting of polyethylene (C_2H_4) and detected at an angle of 40° .

The recorded energy correlation spectra of protons with an incident energy of $E_{\text{kin}} = 106 \text{ MeV}$ (figure 4.9 A) shows two distinct peaks at different energies, which results from elastic scattering processes of the primary protons. The peak at lower energies applies to the scattering on the hydrogen nuclei, the peak at higher energies to the carbon nuclei, which are both included in

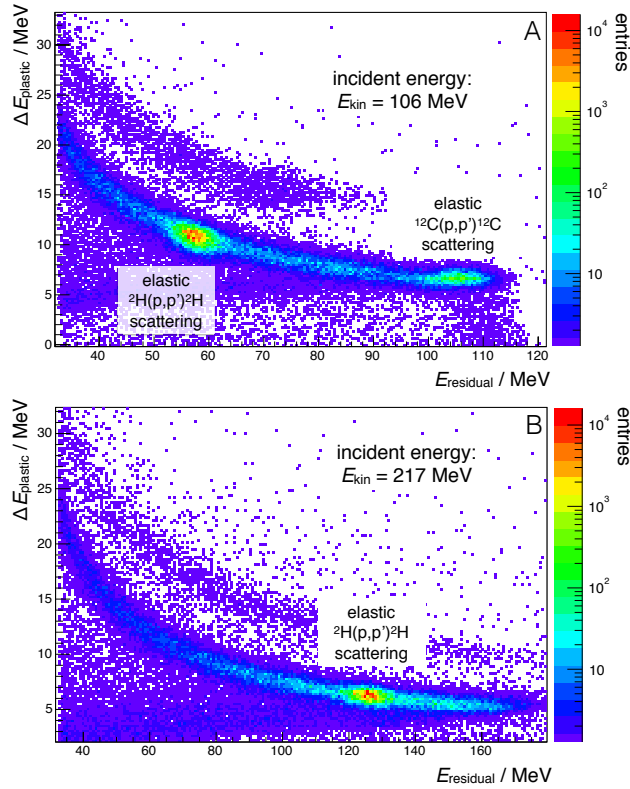


Figure 4.9: The recorded energy correlation spectra shows two distinct peaks at different energies, which results from elastic scattering processes of the primary protons. The peak at lower energies (A) applies to the scattering on the hydrogen nuclei, the peak at higher energies (A,B) to the carbon nuclei, which are both included in the target material.

the target material. Concerning the interaction with the heavy carbon nuclei (atomic mass number of $A = 12$) the transferred energy to the target can be almost neglected. This is in contrast to the scattering on hydrogen, in which the projectile loses approximately half of its energy ($v'_{kin} \approx v_1 \cos(40^\circ) \rightarrow E'_{kin} \approx 0.6 E_{kin}$). Even this respective scattering peak comes out in figure 4.9 B, where the protons have a much higher incident energy ($E_{kin} = 217 \text{ MeV}$). Unlike the peak belonging to the protons scattered on the carbon nuclei, which could not be stopped because of their high kinetic energy.

According to these peak positions a linear energy calibration of the spectrum can be performed by using the elastic scattering formula from section 2.2.2. Figure 4.10 shows the calculated energies correlated to the peaks of different incident energies as a function of the measured channel values for the plastic scintillator and the BGO crystal.

As mentioned in section 2.5 inorganic scintillators have a more linear conversion of the light compared to organic scintillators. This is reflected in the trend of the experimental data, which is absolutely linear for the BGO unlike the data for the plastic component, where the points spread around the linear fit.

Figure 4.11 shows the measured specific energy loss as a function of different incident energies in further experiments after applying the energy calibration from previous measurements (described in the paragraph above). The additional solid line from the National Institute of Standards and Technology (NIST) reference database [10] confirms that the linear calibration of the

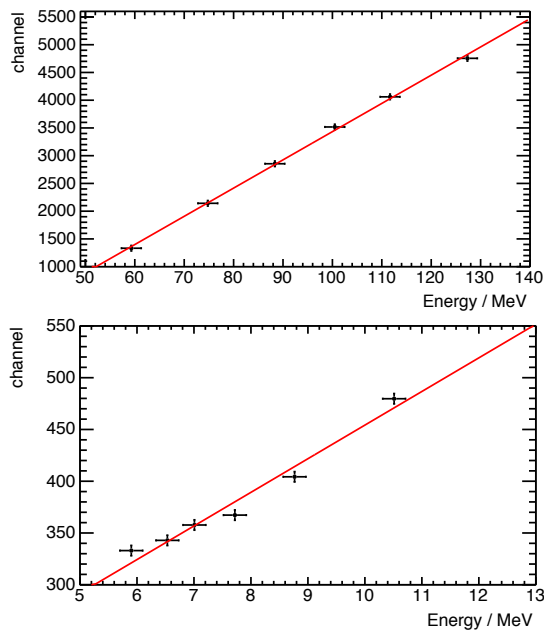


Figure 4.10: Energy calibration based on elastic scattering processes of different incident energies. The calculated energies correlated to the peaks as a function of the measured channel values for the plastic scintillator (right) and the BGO crystal (left).

detector in this energy range is in sufficient agreement with the theoretical calculated values. Consequently, the former channel to energy calibration can be also applied in further experiments if the same operating parameters (e.g. supplying voltage at the PMT) are used, while the desired level of accuracy is retained.

After the energy calibration of the detector it was possible to determine the energy bunch width $\sigma_{\text{energy}}^2 = \sigma_{\text{bunch}}^2 + \sigma_{\text{detector}}^2$. Figure 4.12 shows the correlated full width at half maximum (FWHM) depending on the kinetic energy of the protons scattered at aluminum and copper targets (the energy loss in the foils was neglected).

As expected the energy resolution decreases with higher energies. This is caused by the passive slow down of the protons to reduce their kinetic energy after leaving the cyclotron. The crossing of the extra material (degrader) in the beam line leads to an energy widening of the primary proton bunch. The smaller the requested energy the more material the protons have to pass and the mentioned effect gets a higher impact.

For further timing resolved measurements the digitizer was synchronized by an external clock. As time reference serves the accelerator RF. This allows a straight correlation of the input signal with the cyclotron. For the implementation an update of the digitizer firmware was necessary. Through cooperations with the manufacturer a new firmware was developed and made available by CAEN. The commissioning of the updated version allows first time reference measurements with this type of digitizer. Nevertheless, because of some problems the firmware is still in progress, which requires an continuous exchange between the company and the customer.

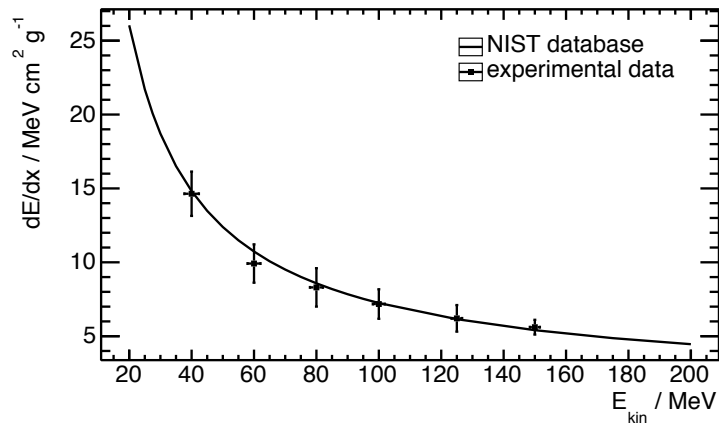


Figure 4.11: The measured specific energy loss as a function of different incident energies after applying the energy calibration from previous measurements. The additional solid line from NIST reference database confirms that the linear calibration of the detector is in sufficient agreement with the theoretical calculated values.

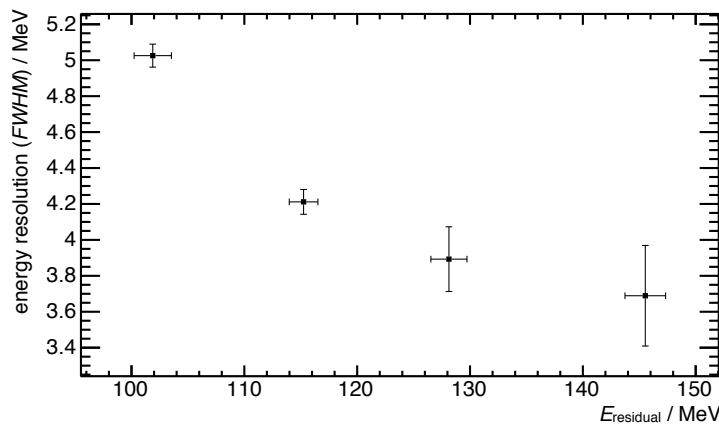


Figure 4.12: Measured energy bunch width of scattered protons as a function of their kinetic energy. The measured *FWHM* includes the detector energy resolution and the energy bunch width.

Particle Identification

To confirm the kind of particle which leads to the additional line (above the proton hyperbole in figure 4.9) in the energy correlation spectra, a time of flight experiment was performed.

A phoswich detector was placed at different distances (figure 4.13) and recorded the time and energy resolved scattering spectra. The requested current at the cyclotron was 5 nA and the acquisition time was set to 2.5 min. The protons were scattered at a copper target ($d = 0.2$ mm).

An identification of the particles can be conducted by measuring the transit time differences related to the protons, which had an initial kinetic energy of $E_{kin} = 217.5$ MeV. Because of the high background it is not possible to extract the arrival time of the other particles directly from the raw spectrum (figure 4.14, 1a).

As described in section 2.6, the hyperboles correlated to the different particles in the energy spectrum are shifted because of mass differences. Therefore, the different particles can be separated by means of PSD (section 3.3) and a more precise arrival time of the respective particles can be determined. Fig-

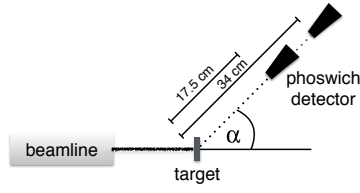


Figure 4.13: Scheme of the experimental setup for time of flight measurements with a phoswich detector placed at different distances ($\alpha = 35^\circ$)

ure 4.14 shows the energy correlation and the energy over time correlation spectra after an energy cut following a hyperbolic function, which defines a minimum/maximum energy for the distinct particles.

The kind of particle, which was detected at several scattering experiments, could be examined by considering the differences in the transit time related to protons, caused by mass differences. The residual kinetic energy deposited in the detector of the elastically scattered protons detected at an angle of 35 degrees is 105 MeV (section 2.2.2). The resulting transit time (section 2.1 equation 2.6, 2.5), to pass the distance from the target to detector in the two different setups (figure 4.13) are $t_p(34 \text{ cm}) = 2.37 \text{ ns}$ and $t_p(17.5 \text{ cm}) = 1.16 \text{ ns}$. These protons were used as reference according to the kinematic of the second particles.

The measured time differences extracted from the recorded energy over time correlation spectra (figure 4.14) of the later arriving particles are $\Delta t_x(34 \text{ cm}) = 0.94 \text{ ns}$ and $\Delta t_x(17 \text{ cm}) = 0.45 \text{ ns}$. The resulting transit times for the second particles are:

$$t_x = t_p + \Delta t_x$$

$$t_x(34 \text{ cm}) = 3.31 \text{ ns} \text{ and } t_x(17.5 \text{ cm}) = 1.63 \text{ ns}.$$

This corresponds to a mass of:

$$m_x = m_p(t_x/t_p)^2$$

$$\bar{m}(34 \text{ cm}) = (1829.6 \pm 240) \text{ MeV}/c^2 \text{ and } \bar{m}(17 \text{ cm}) = (1790.0 \pm 240) \text{ MeV}/c^2.$$

The deuteron has a mass of $m_d = 1875.01 \text{ MeV}/c^2$, which is approximately in the area of the calculated mass. Therefore the second particle hyperbole can be identified as deuteron.

The different time values are also listed in table 4.1.

Table 4.1: Transit time values for protons and secondary particles.

distance	t_p	Δt_x	$t_x = t_p + \Delta t_x$
17.5 cm	2.37 ns	0.45 ns	3.31 ns
34 cm	1.16 ns	0.94 ns	1.61 ns

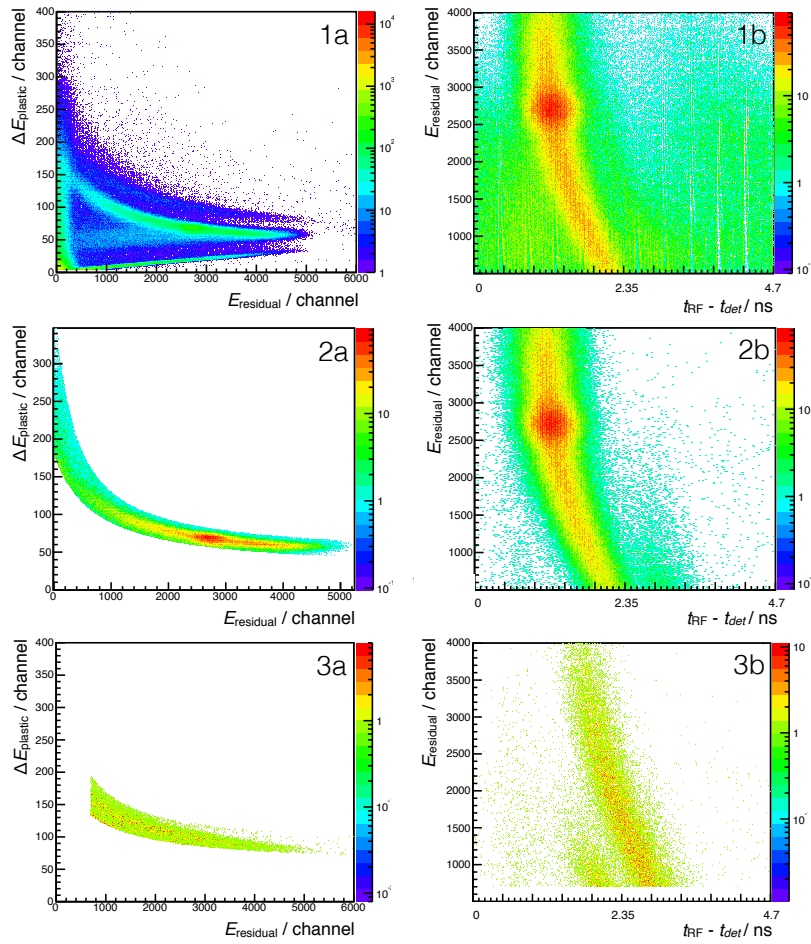


Figure 4.14: The first column shows the energy correlation spectrum with the respective offline PSD-cuts: 1a full energy spectrum, 2a proton energy spectrum, 3a second particle energy spectrum. The second column shows the corresponding energy over time correlation spectrum: 1b full time spectrum, 2b proton time spectrum, 3b second particle time spectrum. These spectrum are recorded with the detector placed in a distance of 34 cm.

4.2.2 Time Width and Yield Measurements

For bunch monitoring purpose, it is important to measure an appropriate number of scattered protons to get a robust estimate of the bunch structure parameters. A high detection efficiency, which implies good statistic, is mainly influenced by the scattering yield, the detector position and the covered solid angle as well as the acquisition time.

In the treatment room, it is not readily possible to place extra scattering material in the beamline. Nevertheless, it could be possible to detect protons scattered at components required for beam formation. This experiment was performed to get a first impression of the expected detecting yield of protons scattered at different target materials.

In the experimental hall, four equivalently designed phoswich detectors placed at different angles and distances (figure 4.15), measured scattered protons of different incident energies. The beam current at the cyclotron was $I(217 \text{ MeV}) = 4 \text{ nA}$, $I(145 \text{ MeV}) = 50 \text{ nA}$ and $I(90 \text{ MeV}) = 100 \text{ nA}$. The measuring time in each setup was 5 minutes.

Additionally, different target compositions i.e. copper (Cu), aluminum (Al) and polyethylene (PE) as scattering bodies were used to determine the yield depending on the properties of the materials. For timing measurements, the digitizer was sampled with twice the cyclotron frequency of 106 MHz (i.e. 212 MS/s).

Figure 4.16 shows the recorded energy correlation and the energy over time correlation spectra for the PE target. The incoming proton energy was 217 MeV. This corresponds to a range in water of 30 cm.

As in earlier experiments, an additional deuteron line was detected. Clearly visible in the trend of the proton line is the elastic scattering peak, where primary protons are scattered at the hydrogen included in the polyethylene.

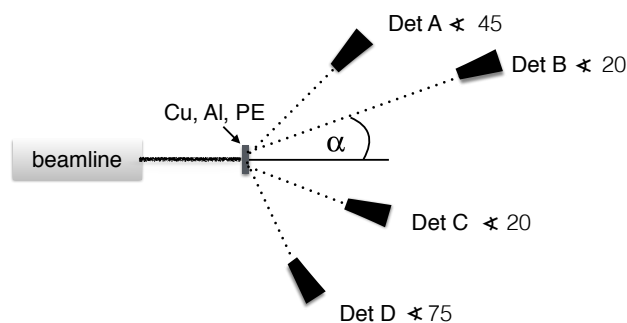


Figure 4.15: Setup of the scattering experiment with four detectors at different positions. Detectors A,B,D are placed at a distance of 30 cm and detector C is located at a distance of 36 cm to the target.

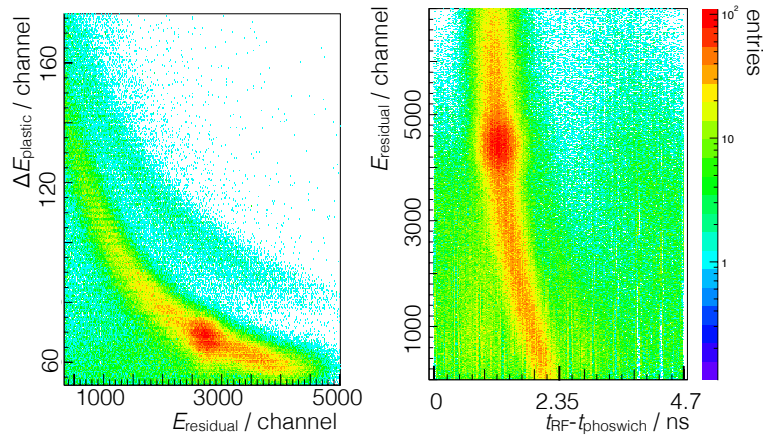


Figure 4.16: Energy correlation and coincidence time spectra of a clinical proton beam at OncoRay, Dresden. Protons ($E_{\text{kin}} = 217$ MeV) scattered on polyethylene were detected at 45° . The timing information of the bunch profile was measured with respect to the accelerator RF.

In figure 4.17, the full width at half maximum ($FWHM_{\text{time}}$) of scattered protons for different incoming energies is shown. Because of the thin targets of Al ($d = 0.1$ mm), Cu ($d = 0.2$ mm) and PE ($d = 1$ mm), the energy loss in the target was neglected. The timing profile of low energy protons (70 MeV) with a $FWHM_{\text{time}} = 1.52$ ns is significantly compressed for higher energies (220 MeV), down to $FWHM_{\text{time}} = 0.46$ ns.

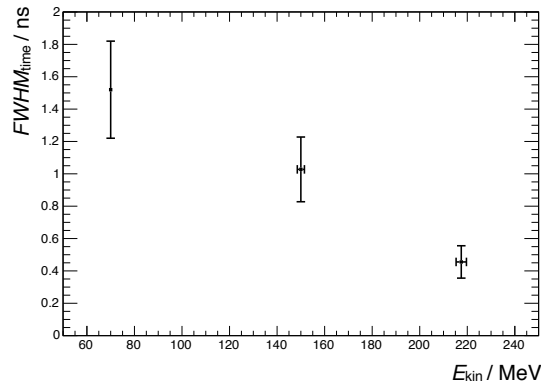


Figure 4.17: The mean $FWHM$ of the timing signal of scattered protons with different incoming energies decreases for a higher primary proton energy.

Figure 4.18 (A) shows the total counts of elastically scattered protons, which encode the bunch structure of the primary protons, on different materials and at different positions with count rates up to 88 kcps. To subtract the background (e.g. due to protons scattered at the exit window, fragmentation, atomic and nuclear de-excitation), a measurement without a target was performed.

The total detection yield differs between the scattering materials. The Cu target, with an atomic mass number of $A = 63$ and a density of $\rho = 8.96$ g/cm³, compared to Al, with an atomic mass number $A = 27$ and a density of $\rho = 2.7$ g/m³ has a significantly higher yield. As expected because of the angular dependence of the cross-section (section 2.2.2), there are also differences

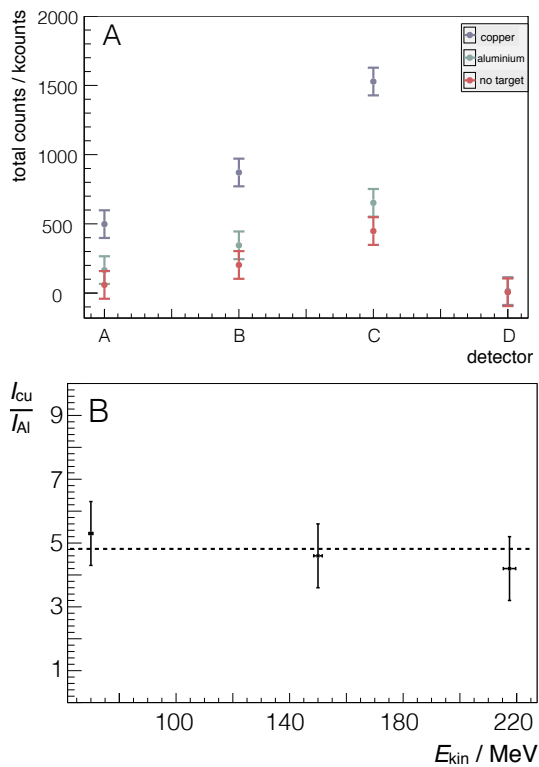


Figure 4.18: A: Total counts of elastically scattered protons on Cu and Al targets. To subtract the background, a measurement without a target was performed. B: The ratio between the total yield of scattered protons detected at $\alpha = 20^\circ$ at a distance of $d = 30$ cm with different energies scattered on Cu and Al foils.

concerning the number of events caused by the different detector angles to the beam line. Detector D at 75° detected less scattered protons than the other detectors at smaller angles. The difference in the total count rate of Detector B and C at 20° results from the different distances ($\Delta d = 6$ cm).

Figure 4.18 (B) shows the ratio between the yield of scattered protons with different energies on Cu and Al. This ratio agrees with the following simple estimation of the cross section [11] with respect to a reference measurement, where r refers to the atomic radius, σ to the cross section and I to the Intensity.

$$r \sim A^{\frac{1}{3}} \rightarrow \sigma \sim A^{\frac{2}{3}} \quad \Rightarrow \quad \frac{I_{Cu}}{I_{Al}} = \frac{d_{Cu} \rho_{Cu} A_{Cu}}{d_{Al} \rho_{Al} A_{Al}} = 4.9.$$

The dashed line in figure 4.18 (right) indicates the calculated ratio $\frac{I_{Cu}}{I_{Al}} = 4.9$. At higher energies, the ratio decreases because of the energy dependent cross section correlation.

4.2.3 Energy Straggling and Detector Timing Resolution

In the last experiment the new firmware update of the DPP-PSD was tested, which allows to improve the acquisition procedure.

For data acquisition an online CFD and PSD-cut was implemented and could be processed by an FPGA. In previous experiments this operations were only possible through an offline procedure.

In contrast to prior experiments a 14 bit digitizer with a maximum sampling rate of 500 MS/s was sampled with 424 MS/s (four times the cyclotron frequency of 106 MHz). This allows a more precise granularity of the analogue waveform, while transferring it to digital data samples. Apart from that, the digitizer has the same features and operation principle as the digitizer used in the previous experiments.

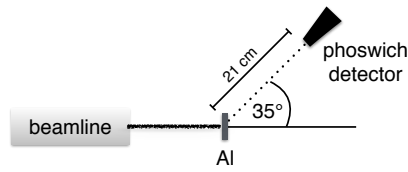


Figure 4.19: Scheme of the experimental setup. Protons were scattered on an aluminum foil and detected at an angle of 35° with a phoswich detector at a distance of 21 cm.

In the experiment protons were scattered on a thin aluminum target ($d = 0.194$ mm) and detected at an angle of 35° . The phoswich detector was placed in a distance of 21 cm. The experimental setup is shown in figure 4.19. The initial kinetic energy of the protons ranges from 90 MeV - 165 MeV and was varied in steps of 5 MeV.

The recorded histograms show the residual energy E_{residual} as a function of the arrival time with respect to the accelerator frequency $t_{\text{det}} - t_{\text{RF}}$. The CFD fraction of the full amplitude was set in the software to a value of 0.75.

An example spectrum generated by scattered protons of an incident energy of $E_{\text{kin}} = 105$ MeV is shown in figure 4.20.

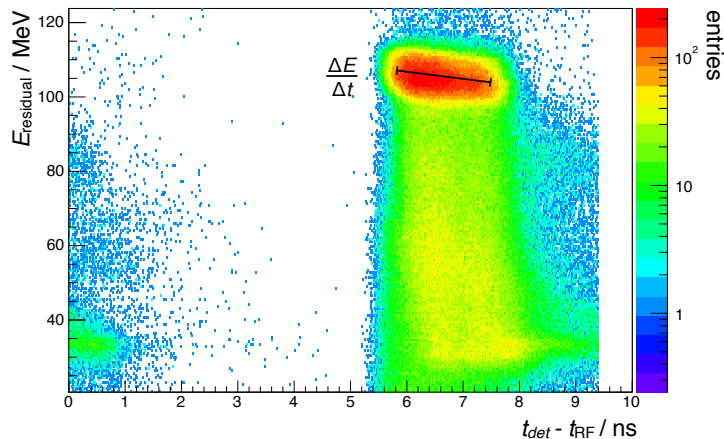


Figure 4.20: The recorded energy over time correlation histograms of 105 MeV protons scattered on an aluminum foil. A slope of the elastically scattering peak can be observed and is marked with a black solid line.

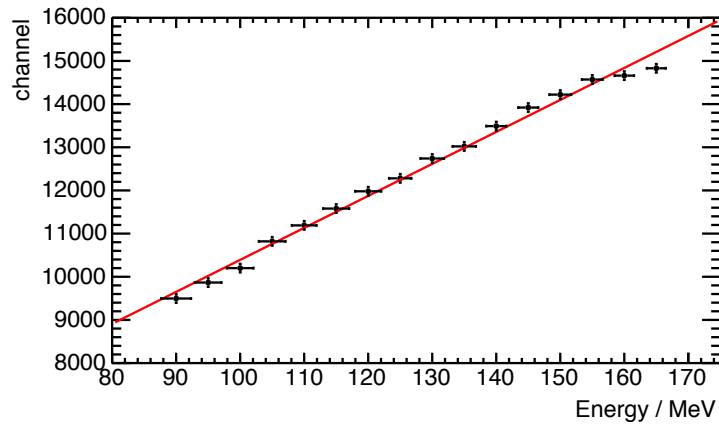


Figure 4.21: For energy calibration the mean peak position as a function of the initial energy was determined and a linear fitted by a linear function.

In the spectrum a drop off of the elastic scattering peak is visible, which is indicated in the figure by a solid line.

As shown in figure 4.21 a linear energy calibration was applied. Therefore the mean peak position of the elastically scattered protons as a function of the initial energy was determined and fitted. The small energy loss in the aluminum foil was neglected.

As mentioned above, the bunch structure influences the recorded spectra, which can be observed especially at the peak originated by the elastically scattered protons. Figure 4.22 illustrates the effect in the spectra for the respective bunch structure parameters. Here, $\Delta t_{\text{initial}}$ is the time spread when the bunch leave the cyclotron. For first estimation the initial time spread was neglected towards the detector time resolution.

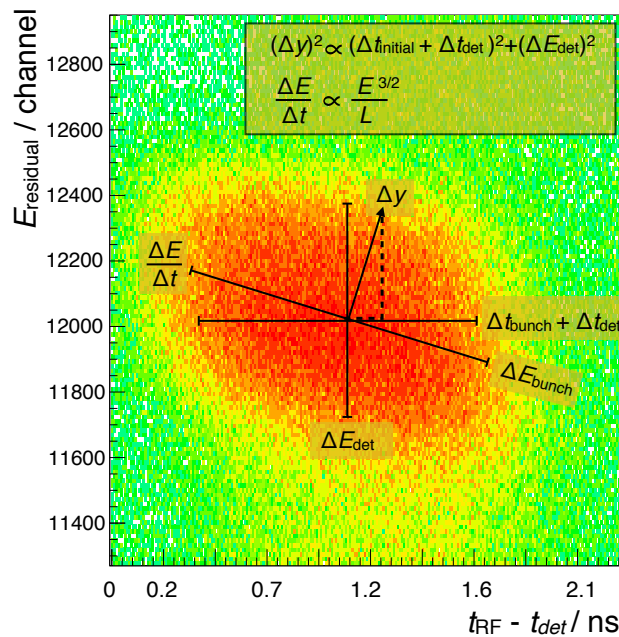


Figure 4.22: Illustration of the effect of the respective bunch structure parameters on the spectra. $L = 27.1$ m: length of the beam line, ΔE_{bunch} : energy bunch width, ΔE_{det} : detector energy resolution, Δt_{bunch} : bunch time width, Δt_{det} : detector timing resolution.

In first approximation the residual energy is proportional to $E_{\text{residual}} \propto 1/t^2$. Because of the energy bunch width ΔE_{bunch} the peak is broadened along these curve (for ΔE_{bunch} small it is approximately linear). The detector energy resolution ΔE_{det} leads to a smearing along the y-axis. Additionally, the bunch time widths Δt_{bunch} and the detector timing resolution Δt_{det} broaden the peak along the x-axis.

The bunch time structure of the scattered protons

$$FWHM_{\text{time}}^2 \propto FWHM_{\text{bunch}}^2 + FWHM_{\text{det}}^2$$

as a function of the kinetic energy of the incoming protons is shown in figure 4.23. As expected from previous measurements the time width decreases with higher energies.

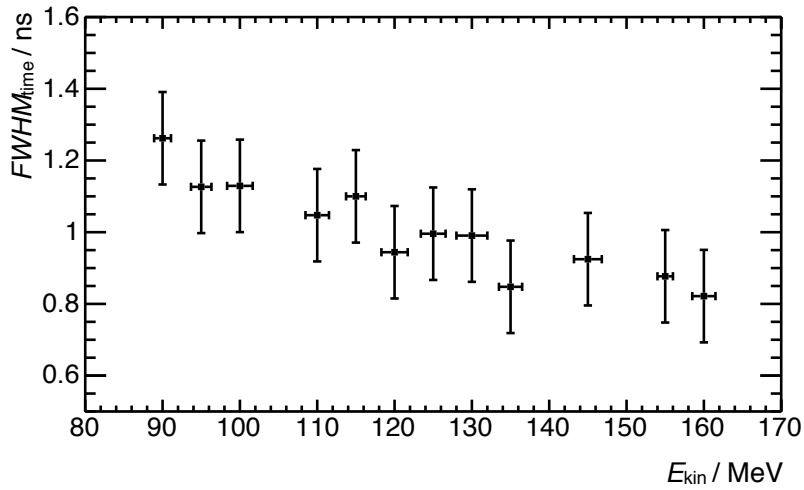


Figure 4.23: The mean $FWHM_{\text{time}}$ of protons scattered on a thin aluminum target for different beam energies.

In the recorded energy over time correlation spectra a drop of the proton peak can be observed. The slope of the elastically scattering peak, which is in first approximation given by

$$\frac{dE}{dt}(E, L) = \frac{-2E^{3/2}}{L} \sqrt{\frac{2}{m}} \quad (4.3)$$

is influenced by the length of the beam line $L = 27.1$ m and the initial kinetic energy E_{kin} . The dispersion of the bunch in the beam line (initial ΔE) leads to an additional time spread. The theoretical values and the experimental values listed in table 4.2, are in good agreement.

Table 4.2: Theoretical and experimental values of the slope of the elastically scattered energy peak.

$E_{\text{kin}}/\text{MeV}$	$dE/dt_{\text{theo}} \text{ MeV ns}^{-1}$	$dE/dt_{\text{exp}} \text{ MeV ns}^{-1}$
155	1.98	1.80
150	1.89	1.72
145	1.79	1.75
125	1.43	1.43
120	1.35	1.35
115	1.27	1.27
110	1.18	1.18
105	1.10	1.07
95	0.95	0.95
90	0.88	0.89

Compared to previous measurements with the same beam setting parameters (current at cyclotron: 10 nA, kinetic energy: 145 MeV) and the same experimental setup (scattering angle: $\alpha = 35^\circ$, distance: $d = 20$ cm) the count rate increases from ~ 6000 cps to ~ 10000 cps. Mainly, because transferring part of the raw waveform for an offline CFD is not longer necessary.

Chapter 5

Conclusion and Outlook

In first experiments the digital acquisition system was tested under different preconditions combined with a NaI(Tl) detector and a self-built phoswich detector. The commissioning of the programmed control software was carried out and important software parameter values were examined. It was possible to record first energy correlation spectra (PSD-plots) of different particles.

Furthermore, time reference measurements with respect to the accelerator frequency combined with an offline CFD algorithm were performed and the time resolution depending on the photon energy were determined.

The measured values are in the same order as in *K. Roemer et al. (2015) [25]*, where the time resolution with a NaI(Tl) detector at ELBE was also measured. For example the measured time resolution are $\sigma_{\text{time}}(1250 \text{ keV}) = 1.9 \text{ ns}$ and $\sigma_{\text{time}}(2750 \text{ keV}) = 1.13 \text{ ns}$ compared to the values presented in section 4.1.2 with $\sigma_{\text{time}}(1250 \text{ keV}) = 1 \text{ ns}$ and $\sigma_{\text{time}}(2750 \text{ keV}) = 0.78 \text{ ns}$. This shows that the system yields an improved resolution even at 250 MS/s.

In further scattering experiments at a clinical cyclotron, a basic energy calibration allows to estimate the energy bunch widths depending on the kinetic energy of the particles. As expected, it increases significantly with a lower kinetic energy of the primary protons due to the energy straggling in the degrader.

Additionally, a time of flight experiment could identify deuterons, which were detected as secondary particles in nearly all scattering spectra.

Besides the energy bunch width, it was determined that the timing resolution depends strongly on the kinetic energy of the scattered protons. The measured bunch time width $\sigma_{\text{time}}(220 \text{ MeV}) = 0.46 \text{ ns}$ is in good agreement with measurements presented in *Petzoldt et al. (2015) [26]*, where the bunch time width during beamtuning of a 225 MeV proton beam was determined with $\sigma_{\text{time}}(220 \text{ MeV}) = 0.4 - 0.50 \text{ ns}$.

As specified in [3], PGT measurements rely on detecting changes in the order of picoseconds in the prompt gamma emission profile. Compared to the presented bunch widths in the range of nanoseconds, it is an important task to measure the timing structure (with a simultaneous discrimination of the timing resolution of the detection system) of the primary particle bunch to correct PGT profiles. Even in clinical applications, no reference values for energy and timing widths of the proton bunches exist. And with regard to an implementation of PGT during patient treatment, it is important to measure the fluctuations of these values.

For bunch monitoring, it is important to detect enough scattered primary protons in order to extract the energy and timing information out of the measured spectra. Besides the beam current, the properties of the scattering material

influences the number of the total detected events. The performed yield measurements with thin materials show that copper with a high density and a high atomic mass number is more suitable as scattering body compared to aluminum. The results of the experiments verify the expected correlation.

In the last experiment a digitizer with a higher sampling rate of 500 MS/s was used for a more precise measurement of the bunch width and makes the system more competitive and robust compared to analog data acquisition.

Additionally, an implementation of the online CFD algorithm and an online PSD-Cut (background discrimination) leads to a significant increase of the data throughput and makes the data acquisition much faster.

A further purpose is the separation of the detector properties, which lead to a convolution of the bunch time and energy spread in the measurements. If the energy and time resolution of the detector is known, their contributions to the measured time and energy widths can be determined. Consequently, the subtraction of the detector parameters from the measured data define the raw bunch time and energy structure.

The recorded energy over time correlation spectra of particles with a different kinetic energy allow a first estimation of the detector time resolution.

As mentioned in section 4.2.3, The slope of the peak $\frac{dE}{dt}(E, L)$ is influenced by the length of the beam line $L = 27.1$ m and the initial energy E . Figure 5.1 shows a graphical comparison of the measured data points (dE/dt_{exp}) and the theoretical expected data (dE/dt_{theo}).

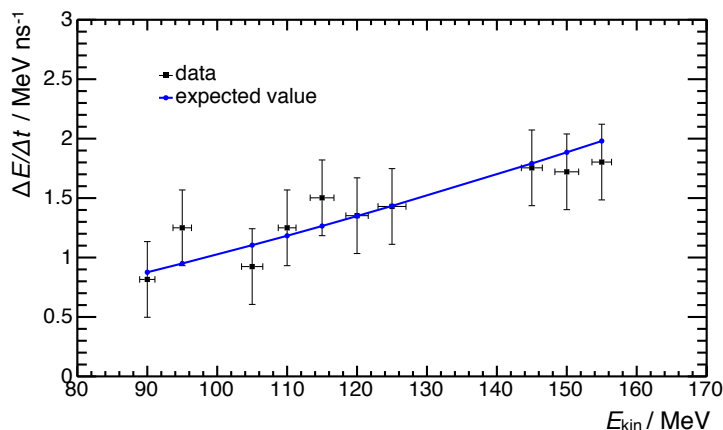


Figure 5.1: The measured slopes of the different energy peaks compared to the calculated values under consideration of the beamline length ($L = 27.1$ m).

The extraction of the detector timing resolution from the measured spectra was exemplary done by taking into account two distinct energy spectra. As referred in section 4.2.3, the perpendicular line Δy to the slope depends on the detector time width and on the detector energy resolution. The detector parameters can be extracted by solving a system of equations with the following structure:

$$\sigma_y^2 = \sigma_E^2 + \left(\frac{dE}{dt}\right)^2 \sigma_t^2 \quad (5.1)$$

from the individual measurements. The extracted value for the detector timing resolution was $FWHM_{\text{time}} = 0.7$ ns.

The timing resolution in [26] of similar phoswich detectors are in the range of $FWHM_{\text{time}} \sim 0.300$ ns. In further analyzes of the measured data, additional

influences should be considered, to retrieve the detector timing resolution more accurately. This could be, for example, the energy straggling in the plastic scintillator component and the different light yield and light collection efficiency in the detector stages, which influences the residual energy.

A further verification of the detector time resolution can be conducted by considering another approach, which is described in *Petzoldt et al., (2015)* [26]. This method is based on coincidence measurements with two identical designed phoswich detectors, which record elastically scattered protons at an angle of 45 degrees (with respect to the beam axis). The measured coincidence resolution time Δt_{crt} includes both detector timing resolutions $\Delta t_{\text{crt}}^2 = \Delta t_{\text{det1}}^2 + \Delta t_{\text{det2}}^2$ and does not depend on the bunch structure. Therefore, it is possible to extract the respective detector timing resolutions. These values can be subtracted from the measured time widths to get finally the bunch time width. A detailed description can be found in [26].

As proved in many scattering experiments, the phoswich detector records spectra of scattered protons in the desired quality for first tests of the bunch monitor system. Due to the detector properties, it was possible to separate the high background in the various scattering experiments and therefore to extract the respective bunch widths.

Because of the self built detector, the system does not provide an optimal light collection. This could be significantly improved by applying a commercially manufactured model with a better finishing and connection of the transitions between the two scintillator materials and the coupling to the PMT.

Besides this, the traveling of the protons through the plastic scintillator, leads to an additional energy straggling until they reach the BGO crystal. A first estimation of this effect can be done by a simulation [27] of the deposited energy in a 0.95 cm plastic scintillator combined with a subsequent 5 cm BGO crystal of mono-energetic (90 MeV) protons. The particles reach the front of the scintillation materials after passing 0.2 mm aluminum and 40 cm air. The sum of the deposit energy in the respective detector stages leads to a sharp energy peak, which means that the energy straggling in air can be neglected. The resulting energy spread, which is therefore mainly caused by the energy straggling in the plastic scintillator, was $FWHM_{\text{energy}} = 1.5$ MeV [27].

The application of other scintillation materials and changes in the geometry (thinner material) could reduce this influence. For example, the use of barium fluoride (BaF_2) is a possible alternative, while the fast time resolution will be maintained.

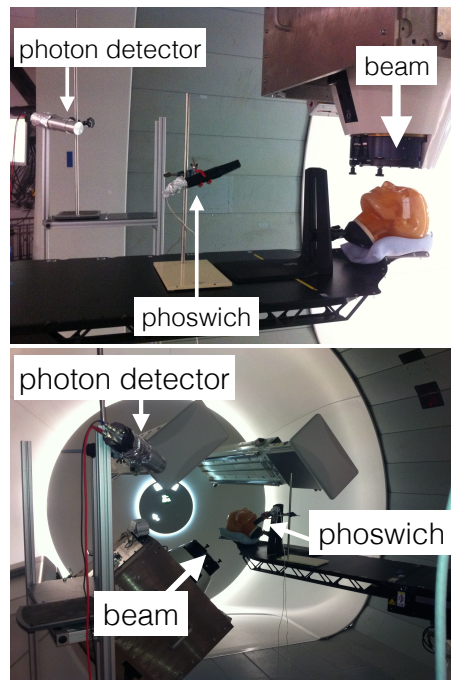


Figure 5.2: Experimental setup in the treatment room at OncoRay Dresden where measurements were performed during workflow training. The phoswich detector was placed in a distance around 60 cm to the gantry nozzle.

The present experimental setup was also tested in the gantry treatment room under clinical conditions. During patient treatment, it is not possible to place extra experimental material in the beamline. As referred in section 4.1, components for beam modeling are placed in the nozzle (at the end of the beamline) for passive field modulation and could act as scattering body. Hence, the next aim is to find out whether enough protons for bunch monitoring are detectable. As shown in figure 5.2 the detectors are placed next to the gantry nozzle. A recorded energy correlation spectra with the typical proton line is shown in figure 5.3.

Considering the detector counting rate as shown in figure 5.4 a periodic behavior of the beam current can be observed. This effect results from the passive field modulation with the help of an rotating modulator wheel. The wheel is made up of steps with different thicknesses, which results in a fluctuation of the count rate.

The first measurements in the treatment room show that it is possible to measure scattered protons and it is additionally possible to get information of the beam setting parameters. An integrated bunch monitor system could be therefore used as an independent control system of the beam.

To get data under clinical conditions, a mini phoswich detector is under construction. It consists of a thin BGO crystal rod combined with a small plastic scintillator rod and it may be installed directly inside the gantry nozzle. This allows a permanent data acquisition during irradiation, without visible experimental instruments. As a light detector system, two variants are under consideration: a silicon photo multiplier (SiPM) and a microPMT (μ PMT) [9], in order to not be sensitive to magnetic fields.

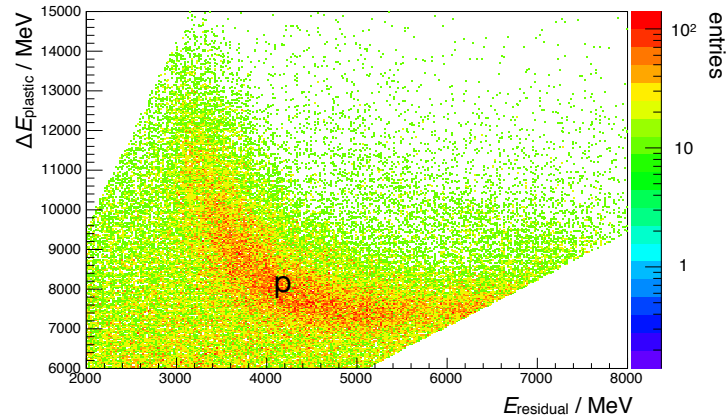


Figure 5.3: Energy correlation spectra of scattered protons extracted from the nozzle in the treatment room.

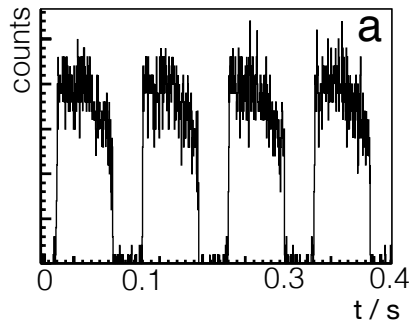


Figure 5.4: The count rate reflects the current and energy regulation for the homogeneous dose distribution. The beam starts and stops at a special position at the modulator wheel.

The results of the experiments show that it is possible to employ the presented experimental setup as a bunch monitor system. One advantage of the system is the high flexibility due to the compact setup, which is easy to handle and can be quickly installed nearly independent of the outer medical circumstances. Additionally, it is a low cost variant to perform the presented measurements. Furthermore, the setting of the acquisition parameters in the software do not disturb the experimental work flow and allows a fast response concerning changes during the experiment (e.g. beam current, particle energy, acquisition time, background). Anyway, compared to analog detection systems it demands a high level of programming effort and fundamental knowledge of the operation principle of the digitizer.

At the digitizer up to 8 detectors for different application in particle detection can be connected. This combined with the various features of the acquisition system makes it usable in wide areas. This could include for example simple energy spectroscopy (figure 5.5 top) or more complex energy and time reference measurements (figure 5.5 bottom) .

Another special property, which can be implemented in the digitizer firmware is the online coincidence modus. The coincidence algorithm determines the time difference between two events. If it is less than a certain time window (resolving time) the corresponding event is saved. For high rate input signals

the system is setup to trigger online on coincident events to reduce the read-out rate. Especially, PET-applications, where coincidence events are used for imaging, could take benefit of this feature.

Finally, the presented studies of a proton bunch monitor system for range verification in proton therapy demonstrate the high potential regarding future investigations of beam structure parameters (e.g. energy and time width of the bunch).

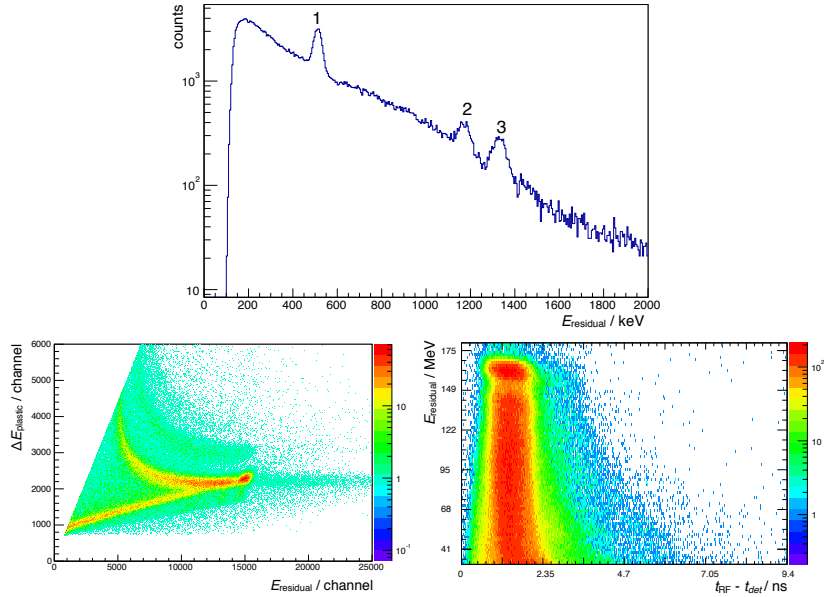


Figure 5.5: Various spectra measured with the digital data acquisition system. The various features of the acquisition system makes it usable for example in simple energy spectroscopy. The upper picture shows a 1D energy spectrum measured in a scattering experiment with an additional cobalt source in front of the detector. The energy peaks are 511 keV (1), 1173 keV (2) and 1332 keV (3). Additionally, it is possible to record more complex energy and time reference measurements. The bottom figures show energy correlation and energy over time correlation spectra of protons.

Bibliography

- [1] H. Paganetti, *Proton Therapy Physics*. Series in Medical Physics and Biomedical Engineering. CRC Press, Massachusetts General Hospital and Harvard Medical School, Boston, USA, (2012).
- [2] H. Paganetti, *Range uncertainties in proton therapy and the role of Monte Carlo simulations*, Physics in Medicine and Biology **57** no. 11, (2012) R99. <http://stacks.iop.org/0031-9155/57/i=11/a=R99>.
- [3] K. Parodi and W. Enghardt, *Potential application of PET in quality assurance of proton therapy*, Physics in Medicine and Biology **45** no. 11, (2000) N151. <http://stacks.iop.org/0031-9155/45/i=11/a=403>.
- [4] J. Smeets, F. Roellinghoff, D. Prieels, F. Stichelbaut, A. Benilov, P. Busca, C. Fiorini, R. Peloso, M. Basilavecchia, T. Frizzi, J. C. Dehaes, and A. Dubus, *Prompt gamma imaging with a slit camera for real-time range control in proton therapy*, Physics in Medicine and Biology **57** no. 11, (2012). <http://stacks.iop.org/0031-9155/57/i=11/a=3371>.
- [5] G. Llosá, J. Cabello, S. Callier, J. E. Gillam, C. Lacasta, M. Rafecas, L. Raux, C. Solaz, V. Stankova, C. de La Taille, M. Trovato, and J. Barrio, *First Compton telescope prototype based on continuous LaBr₃-SiPM detectors*, Nuclear Instruments and Methods in Physics Research A **718** (2013) 130–133.
- [6] F. Fiedler, U. Dersch, C. Golnik, T. Kormoll, A. Muller, H. Rohling, S. Schone, and W. Enghardt, *The use of prompt gamma-rays for in-vivo dosimetry at therapeutic proton and ion beams*, Nuclear Science Symposium and Medical Imaging Conference (NSS/MIC), 2011 IEEE (2011) 4453–4456.
- [7] F. Hueso-González, W. Enghardt, F. Fiedler, C. Golnik, G. Janssens, J. Petzoldt, D. Prieels, M. Priegnitz, K. E. Römer, J. Smeets, F. V. Stappen, A. Wagner, and G. Pausch, *First test of the prompt gamma ray timing method with heterogeneous targets at a clinical proton therapy facility*, Physics in Medicine and Biology, accepted (2015).
- [8] J. Petzoldt, K. Roemer, T. Kormoll, M. Berthel, A. Dreyer, W. Enghardt, F. Fiedler, F. Hueso-Gonzalez, C. Golnik, T. Kirschke, A. Wagner, and G. Pausch, *Fast Timing with BGO (and other Scintillators) on digital Silicon Photomultipliers for Prompt Gamma Imaging*, IEEE NSS/MIC, Conf. Rec. (2014).
- [9] T. Bortfeld and W. Schlegel, *An analytical approximation of depth - dose distributions for therapeutic proton beams*, Physics in Medicine and Biology **41** no. 8, (1996) 1331. <http://stacks.iop.org/0031-9155/41/i=8/a=006>.

- [10] M. Berger, *ESTAR, PSTAR, and ASTAR: Computer Programs for Calculating Stopping-Power and Range Tables for Electrons, Protons, and Helium Ions (version 1.2.3)*, (2015).
<http://physics.nist.gov/Star>.
- [11] B. Povh, K. Rith, C. Scholz, F. Zetsche, and W. Rodejohann, *Teilchen und Kerne: Eine Einführung in die physikalischen Konzepte*. Springer-Lehrbuch. Springer Berlin Heidelberg, (2013).
- [12] Particle Data Group Collaboration, K. A. Olive et al., *Review of Particle Physics*, *Chin. Phys.* **C38** (2014) 090001.
- [13] K. Bethge, G. Walter, and B. Wiedemann, *Kernphysik: Eine Einführung*. Springer-Lehrbuch. Springer Berlin Heidelberg, (2007).
<http://books.google.de/books?id=1U-0Eqs0YykC>.
- [14] J. S. U. L. de Bruxelles, *Prompt gamma imaging with a slit camera for real time range control in particle therapy*. PhD thesis, Universite Libre de Bruxelles, 2012.
- [15] C. Golnik, F. Hueso-González, A. Müller, P. Dendooven, W. Enghardt, F. Fiedler, T. Kormoll, K. Roemer, J. Petzoldt, A. Wagner, and G. Pausch, *Range assessment in particle therapy based on prompt gamma-ray timing measurements*, *Physics in Medicine and Biology* **59** no. 18, (2014). <http://stacks.iop.org/0031-9155/59/i=18/a=5399>.
- [16] G. F. Knoll, *Radiation detection and measurement*. Wiley, New York, NY, 4 ed., (2010).
- [17] N. Akchurin, F. Bedeschi, A. Cardini, M. Cascella, G. Ciapetti, D. D. Pedis, M. Fasoli, R. Ferrari, S. Franchino, M. Fraternali, G. Gaudio, J. Hauptman, M. Incagli, F. Lacava, L. L. Rotonda, S. Lee, M. Livan, E. Meoni, A. Negri, D. Pinci, A. Policicchio, F. Scuri, A. Sill, G. Susinno, and T. Venturelli, *A comparison of BGO and BSO crystals used in the dual-readout mode*, *Nuclear Instruments and Methods in Physics Research A* (2011).
- [18] D. H. Wilkinson, *The Phoswich-A Multiple Phosphor*, *Review of Scientific Instruments* **23** (1952) 414–417.
- [19] C. Pastor, F. Benrachi, B. Chambon, D. Drain, A. Dauchy, A. Giorni, and C. Morand, *Detection of charged particles with a phoswich counter*, *Nuclear Instruments and Methods in Physics Research* **212** (1983) 209–215.
- [20] S. Tang, C. Deville, Z. Tochner, K. K.-H. Wang, J. McDonough, N. Vapiwala, and S. Both, *Impact of Intrafraction and Residual Interfraction Effect on Prostate Proton Pencil Beam Scanning*, *International Journal of Radiation Oncology* **90** no. 5, (2015) 1186–1194.
<http://dx.doi.org/10.1016/j.ijrobp.2014.08.015>.
- [21] CAEN, *Technical Information Manual UM2580*, revision n. 9 ed., July, (2014).
- [22] A. Wagner, R. Beyer, M. Erhard, F. Dönau, E. Grosse, A. Hartmann, A. R. Junghans, L. Käubler, K. Kosev, S. Mallion, C. Nair, N. Nankov, G. Rusev, K. D. Schilling, W. Schulze, and R. Schwengner, *The new bremsstrahlung facility at the superconducting electron accelerator ELBE*, *Journal of Physics G: Nuclear and Particle Physics* **31** no. 10, (2005) S1969. <http://stacks.iop.org/0954-3899/31/i=10/a=112>.

- [23] F. Hueso-González, C. Golnik, M. Berthel, A. Dreyer, W. Enghardt, F. Fiedler, K. Heidel, T. Kormoll, H. Rohling, S. Schöne, R. Schwengner, A. Wagner, and G. Pausch, *Test of Compton camera components for prompt gamma imaging at the ELBE bremsstrahlung beam*, Journal of Instrumentation **9** no. 05, (2014) P05002. <http://stacks.iop.org/1748-0221/9/i=05/a=P05002>.
- [24] E. Brot, *Some reliability issues of accelerators for proton-therapy*, tech. rep., Institut Curie - Centre de Protonthérapie, (2013).
- [25] K. Roemer, G. Pausch, D. Bemmerer, M. Berthel, A. Dreyer, C. Golnik, F. Hueso-González, T. Kormoll, J. Petzoldt, H. Rohling, P. Thirolf, A. Wagner, L. Wagner, D. Weinberger, and F. Fiedler, *Characterization of Scintillator Crystals for Usage as Prompt Gamma Monitors in Particle Therapy*, submitted to Journal of Instrumentation (2015).
- [26] J. Petzoldt, K. Roemer, W. Enghardt, F. Fiedler, C. Golnik, F. Hueso-González, S. Helmbrecht, T. Kormoll, H. Rohling, T. Werner, and G. Pausch, *Measurements of the Microbunch Time Structure of Proton Pencil Beams at a Clinical Treatment Facility*, to be submitted to Physics in Medicine and Biology (2015).
- [27] T. Kormoll, *Simulation with Geant4 Version 10.2.*, private communication (2015).

BIBLIOGRAPHY

Erklärung

Hiermit erkläre ich, dass ich diese Arbeit im Rahmen der Betreuung am Institut für Kern- und Teilchenphysik ohne unzulässige Hilfe Dritter verfasst und alle Quellen als solche gekennzeichnet habe.

Name
Ort, Datum